# Nitro-oxidized Carboxycellulose Nanofibers From Moringa Plant: Effective Bioadsorbent for Mercury Removal

**HUI CHEN**
Stony Brook University https://orcid.org/0000-0003-3337-0975
**Sunil K. Sharma**
Stony Brook University College of Arts and Sciences
**Priyanka R. Sharma**
Stony Brook University College of Arts and Sciences
**Kai Chi**
Stony Brook University College of Arts and Sciences
**Eric Fung**
Stony Brook University College of Arts and Sciences
**Katherine Aubrecht**
Stony Brook University College of Arts and Sciences
**Ngonye Keroletswe**
Botswana Institute for Technology Research and Innovation
**Samuel Chigome**
Botswana Institute for Technology Research and Innovation
**Benjamin S Hsiao** ( benjamin.hsiao@stonybrook.edu )
Department of Chemistry Stony Brook University Stony Brook, New York

**Research Article**

**Keywords:** Nitro-oxidization, cellulose nanofibers, mercury removal, moringa, adsorption, mineralization

**Posted Date:** April 2nd, 2021

**DOI:** https://doi.org/10.21203/rs.3.rs-368266/v1



**Version of Record:** A version of this preprint was published at Cellulose on July 14th, 2021. See the published version at https://doi.org/10.1007/s10570-021-04057-5.

# Nitro-oxidized Carboxycellulose Nanofibers from Moringa Plant: Effective Bioadsorbent for Mercury Removal

Hui Chen[1†], Sunil K. Sharma[1†], Priyanka R. Sharma[1*], Kai Chi[1], Eric Fung[1], Katherine Aubrecht[1], Ngonye Keroletswe[2], Samuel Chigome[2], Benjamin S. Hsiao[1]*

[1] Department of Chemistry

Stony Brook University

Stony Brook, New York 11794-3400, United States

[2] Botswana Institute for Technology Research and Innovation

Private Bag 0082

Gaborone, Botswana

[†] Authors HC and SKS have equal contribution.

* Corresponding authors.

PRS: Tel: +16315423506, E-mail: priyanka.r.sharma@stonybrook.edu;

BSH: Tel: +16316327793, E-mail: benjamin.hsiao@stonybrook.edu

## Abstract

Mercury contamination in drinking water is a worldwide problem due to its severely harming effects on the human body. A nanostructured natural bioadsorbent, carboxycellulose nanofiber extracted from raw moringa plant using the nitro-oxidation method (termed NOCNF), capable of effectively remediating this problem has been demonstrated. Nitro-oxidation is a simple approach that can extract carboxylated nanocellulose directly from raw biomass. In this study, the produced NOCNF contained a large density of carboxylate groups on the cellulose surface (0.97 mmol/g), capable of removing $Hg^{2+}$ ions by simultaneous electrostatic-interactions and mineralization processes. Using the Langmuir analysis, the adsorption results indicated that the highest $Hg^{2+}$ removal capacity of this NOCNF was 257.07 mg/g, which is higher than most of the reported values. The interactions between $Hg^{2+}$ and NOCNF were further characterized by Fourier-transform infrared spectroscopy (FTIR), scanning electron microscopy/energy dispersive spectroscopy (SEM/EDS), transmission electron microscopy (TEM) with electron diffraction and wide-angle X-ray diffraction (WAXD) methods, suggesting the existence of two distinct removal mechanisms: predominant adsorption at low $Hg^{2+}$concentrations (< 250 ppm) and predominant mineralization at high $Hg^{2+}$ concentrations (> 1000 ppm). The applications of NOCNF were illustrated in both suspension form, as an adsorbent/coagulant, and dry powder form using filtration column. The results indicated that NOCNF in suspension exhibited a higher maximum removal efficiency of 81.6 % as compared to the dry state of 74.3 %. This work demonstrated the feasibility of extracting nanostructured adsorbents from biomass feedstocks to tackle the $Hg^{2+}$ contamination problem in drinking water.

**Keywords**

Nitro-oxidization, cellulose nanofibers, mercury removal, moringa, adsorption. mineralization

**Declarations**

Funding is from National Science Foundation (DMR-1808690); Authors have no conflicts of interest; Data and material are all transparent.

## Introduction

Mercury is a well-recognized harmful pollutant due to its carcinogenicity, mutagenicity and teratogenicity.(Zhang, Nriagu et al. 2005) For example, high concentration of mercury in the human body can cause tyrosinemia, a disease associated with impairment of pulmonary and kidney function, chest pain and dyspnea. One main source of the mercury intake is through the consumption of contaminated fish. In 1956, a horrifying 'Minamata disaster' occurred in Japan, where people had unknowingly consumed shellfishes contaminated with mercury.(Harada 1995, Rio and Delebarre 2003) Although it has been more than 50 years since the incident, many victims still suffer irreversible damage in their central nervous system. This is because mercury ions can bind to varying proteins in the nervous and renal systems, leading to permanent injury. (Lai, Wong et al. 1993)

Due to the acute health threats to humans, the EPA permitted discharge limit of the total mercury amount in wastewater is 10 mg/L, where the limit for drinking water is 2 mg/L.(Nam, Gomez-

Salazar et al. 2003)-(Zabihi, Ahmadpour et al. 2009) Meanwhile, the Word Health Organization (WHO) recommends a maximum uptake of 0.3 mg per week at 1 mg/L as the maximum acceptable concentration in drinking water.(Zhang, Nriagu et al. 2005) Mercury pollution in the aquatic environment is commonly generated from chloralkali plants, paper and pulp industries, oil refining, electrical, rubber processing and fertilizer industries.(Baeyens, Ebinghaus et al. 1997, Chiarle, Ratto et al. 2000) A plenty of physical and chemical strategies have been investigated and applied for mercury remediation in contaminated drinking water, such as solvent extraction, ion-exchange, precipitation, membrane separation, reverse osmosis, coagulation and photoreduction.(International Symposium on Metals Speciation, Recovery et al. , Larson and Wiencek 1992, Skubal and Meshkov 2002) These methods often require either high consumption of energy or usage of large quantitiy of chemicals. Among these methods, adsorption/coagulation is perhaps one of the more cost-effective techniques for mercury removal. For example, activated aluminum or activated carbons have been used as effective adsorbents for mercury removal in drinking water purification, however, it is still relatively expensive for large-scale operation. (Di Natale, Erto et al. 2011)

To tackle this problem, we argue that lignocellulosic biomass is an abundant and sustainable resource to develop cost-effective bioadsorbent. (Kim, Shim et al. 2015) In the past two decades, much attention has been given to develop nanocellulose in a broad range of water purification treatments because of its large surface areas and ample functional groups. (Wang 2019) For example, several studies have been reported that cellulosic nanomaterials containing thiol, carboxyl, sulfonate, and phosphonate groups can all exhibit ability to adsorb positively charged contaminants, such as metal ions, dyes, and chemicals for water purification. (Wang, Guan et al.

2013, Suman, Kardam et al. 2015, Zhu, Dobryden et al. 2015, Liu, Oksman et al. 2016, Sehaqui, Mautner et al. 2016, Thakur and Voicu 2016, Chen, Sharma et al. 2019, Sharma, Sharma et al. 2020)

Recently, a new method to extract carboxylated cellulose nanofiber from raw biomass using nitric acid ($HNO_3$) and sodium nitrite ($NaNO_2$) mixtures has been demonstrated by our team (we termed this nitro-oxidation process or NOP).(Sharma, Joshi et al. 2017, Sharma, Zheng et al. 2018) The method combines the steps of pulping (delignification) and cellulose oxidation. The proposed mechanisms of NOP are as follows. Nitric acid can facilitate the defibrillation process of raw biomass by degrading non-cellulosic components, such as lignin and hemicellulose, while the generation of $NO^+$ ions (by reaction between $HNO_3$ and $NaNO_2$) can selectively oxidize the primary hydroxyl groups of the cellulose to introduce negatively charged surface to induce defibrillation. Compared with conventional methods, such as TEMPO-mediated oxidation and carboxymethylation processes, the NOP does not require any pretreatments such as alkali and bleaching to obtain cellulosic materials first, thus largely reducing the consumption of energy, water and chemicals. In addition, the effluent from this process can be neutralized into nitrogen salts as plant fertilizers. (Sharma, Joshi et al. 2017) In our application studies, nitro-oxidized cellulose nanofibers (NOCNF) have been found as an effective adsorbent/coagulant to remove toxic metal ions such as cadmium(Sharma, Chattopadhyay et al. 2018), lead(Sharma, Chattopadhyay et al. 2018), and uranium(Sharma, Chattopadhyay et al. 2017, Sharma, Sharma et al. 2020) from water.

In this study, we report that NOCNF, extracted directly from raw moringa plants by NOP, can also be an effective bioadsorbent for water remediation such as mercury removal. Moringa plant is is a native species in parts of Africa and Asia, and its products have well-known antifungal, antiviral, antidepressant, and anti-inflammatory properties. In specific, seeds from Moringa tree have been shown to have unique water purification properties.(Kalibbala, Wahlberg et al. 2009) Here we investigate if the moringa plant itself can be a suitable feedstock for preparing the adsorbents. This is because the hemicellulose content of moringa plant is relatively high (~45 %) (Melesse and Berihun 2013), which can facilitate the defibrillation process in NOP to produce cellulose nanofibers. For the mercury remediation study, we demonstrate the effectiveness of moringa-derived NOP as adsorbents in two different forms: suspension form as typical absorbent/coagulant, and dry form as adsorbent substrate in filtration column. The study also examines the adsorption mechanisms of the mercury removal by the oppositely charged NOCNF. We demonstrate that at low $Hg^{2+}$ concentrations (< 250 ppm), the removal process is mainly dominated by the electrostatic interactions between $Hg^{2+}$ and $COO^-$ on the NOCNF surface, where at high $Hg^{2+}$ concentrations (> 1000 ppm), the removal process is dominated by the mineralization of HgO nanocrystals in the coagulated NOCNF scaffold.

## Experimental Part

### *Materials*

Crushed moringa straw samples, without any pretreatments, from Botswana was used as the biomass feedstock. Nitric acid (ACS reagent, 60 %), sodium nitrite (ACS reagent ≥ 97 %), mercury

acetate, sodium hydroxide, hydrochloric acid (36% assay) chemicals were purchased from the Fisher Scientific. All chemicals were used without any further purification.

***Extraction of NOCNF from Moringa Plant***

NOCNF extracted from moringa feedstock were carried out using NOP with procedures similar to those reported earlier. (Sharma, Joshi et al. 2017) In brief, 2 g of raw moringa sample was placed in a three-neck round bottom flask , where 28 mL nitric acid (60 wt.%, 0.365 mol) was added slowly to completely wet and immerse the biomass. Subsequently, 6.957 mmol of sodium nitrite (0.96 g) was added to the mixture under continuous stirring. Upon addition of sodium nitrite, red gases ($NO_X$) were formed. The mouths of flask were covered with glass stoppers immediately to stop gases from leaking. The reaction was performed at 40 °C for 16 h followed by quenching using 250 mL of distilled water to stop the reaction. The product was settled down under gravity and the supernatant was decanted off to remove the mixture of excessive acid, degraded lignin and oligosaccharides. The above step of decantation process was repeated for 2-3 times until the fibers started to suspend in water. After that, the fibers were centrifuged at 3000 rpm for 10 min, till the pH of supernatant reached above 2.5. Then, the fibers were transferred to a dialysis bag (6-8 kDa) for dialysis until the conductivity of water reached below 5 µS. The extracted fibers contained carboxyl groups (COOH), which were subsequently converted to carboxylate groups ($COO^-$) by treatment with 8% of sodium bicarbonate. The fibers were again introduced to dialysis until the conductivity of dialysis water reached below 5 µS. Finally, the fibers were fibrillated to nanocellulose by passing the 0.2 wt% fiber suspension through a high pressure homogenizer at 250 bar for 1 cycle. The yield of NOCNF obtained was 50 wt%.

***Sample Characterization***

The raw moringa samples and extracted NOCNF were characterized using Fourier transform infrared spectroscopy (FTIR, PerkinElmer Spectrum One instrument-ATR mode), conductometric titration, thermogravimetric analysis (TGA, PerkinElmer STA-6000), transmission electron microscopy (TEM, FEI Tecnai G2 Spirit BioTWIN instrument), atomic force microscopy (AFM, Bruker Dimesion ICON scanning probe microscope), scanning electron microscopy (SEM, Zeiss LEO 1550 SFEG-SEM) with energy dispersive X-ray spectroscopy (EDS) capability, and wide angle X-ray diffraction (WAXD, Benchtop Rigaku MiniFlex 600). The detailed descriptions of these techniques are outlined in the *Supporting Information (SI)*.

The major chemical compositional analysis (i.e., cellulose, hemicellulose, lignin, ash, and extractives) of raw moringa sample and NOCNF was performed by the Celignis Company in Ireland. The analysis was in accordance with the US standard, i.e., NREL standard laboratory analytical procedure TP-510-42623.(Sluiter, Hames et al. 2010) In brief, the following analytical procedures were carried out: (1) acid hydrolysis of samples, (2) determination of acid soluble lignin (ASL) using UV-Vis spectroscopy, (3) gravimetric determination of klason lignin (KL), and (4) chromatographic analysis of hydrolysate.

***Mercury Remediation Study***

Mercury Adsorption by NOCNF in Suspension

In this study, $Hg^{2+}$ solutions with concentrations ranging from 2.5 to 1000 ppm were first prepared, where these solutions were subsequently mixed with a NOCNF suspension as an adsorbent/coagulant. In specific, 2 mL of heavy metal stock solution (2.5 to 1000 ppm) was slowly added with 2 mL of NOCNF suspension (0.40 wt%) in a test tube. Upon mixing, the floc, containing both aggregated Hg and NOCNF components, was formed and settled down to the bottom of the tube. The non-flocculated supernatant was then passed through a 0.22 μ filter to remove any fiber residues, but not $Hg^{2+}$ ions. The obtained solution was diluted before submitting for ICP-MS measurements.

Additionally, the effect of pH on the adsorption of $Hg^{2+}$ by NOCNF was investigated. In this evaluation, 100 ppm $Hg^{2+}$ solutions at different pH values: 3, 5, 7, 9 and 11, were prepared. Subsequently, 2 mL of NOCNF suspension was added to 2 mL of varying $Hg^{2+}$ solutions. Similar to the above procedure, the non-floc portion were extracted, diluted 1000 times and filtered through a 0.22 μ filter for ICP-MS analysis. The ICP-MS results were used to calculate the mercury removal efficiency of NOCNF.

The $Hg^{2+}$ adsorption evaluation of NOCNF was performed by using the data obtained from the ICP-MS analysis. In specific, the adsorption capacity at equilibrium (*Qe*) and equilibrium concentration of adsorbate (*Ce*) were calculated, where their relationship was evaluated by using both Langmuir and Freundlich isotherm models. The Langmuir model is based on the assumption of monolayer adsorption on the active site of the adsorbent, whereas the Freundlich model is based

on the assumption of multilayer adsorption on the active site of the adsorbent. The Langmuir model can be expressed as follows.

$$\frac{Ce}{Qe} = \frac{Ce}{Qm} + \frac{1}{Qmb} \qquad \text{Eq. 1}$$

where *Qm* (the maximum adsorption capability) and *b* (the Langmuir constant) can be calculated from the intercept and the slope of the *Ce*/*Qe* versus *Ce* plot. (Wang and Kuo 2007) In contrast, the Freundlich model can be expressed as follows.

$$\lg Qe = \frac{1}{n}\lg Ce + \lg K_f \qquad \text{Eq. 2}$$

where $K_f$ and *n* are characteristic constants of the system. (Cui, Liu et al. 2016)

Characterization of Hg-NOCNF Floc

The floc samples formed from the mixing of $Hg^{2+}$ solutions and NOCNF suspension were characterized by different techniques including FTIR, TEM with electron diffraction, SEM/EDS and WAXD to determine the mechanisms of the mercury removal by NOCNF. In addition, the hydrophobicity of the floc sample was analyzed by an optical contact angle meter (CAM200, KSV instruments, LID), which is described in the *Supporting Information* (SI).

Preparation of Filtration Column for Dry NOCNF Adsorbent

The filtration column using freeze dried NOCNF samples was also carried out to test the $Hg^{2+}$ removal efficiency. In specific, 3 g of dried NOCNF samples was used to fill a filtration column of 3 cm in diameter and 25 cm in length. Subsequently, a 100 ppm $Hg^{2+}$ solution was added to the

top of the column to initiate the test. A total number of 10 additions with an increment of 15 mL of $Hg^{2+}$ solution for each addition was poured into the column, and the output filtrate obtained from bottom was collected and labeled accordingly. The filtrate was diluted 1000 times and then submitted for ICP-MS measurements. The removal efficiency from the solid NOCNF form in the filtration column was compared with that from the dispersed NOCNF form in suspension.

## Results and Disscussion

### *Chemical Composition Analysis*

Similar to other cellulose nanofibrils (such as TEMPO-CNF), the 0.4 wt% NOCNF suspension was translucent and showed viscous and gel-like behavior (as seen in the inset image in Figure 1). This indicates that the nitro-oxidation process is an efficient pathway to defibrillate raw moringa plant even without pretreatments (or delignification step). The chemical compositions of the raw moringa plant and resulting NOCNF were quantitively characterized, and the results are shown in Figure 1. It was seen that the holocellulose (cellulose and hemicellulose), lignin (acid soluble lignin (ASL) and klason lignin (KL)), ash and extractives contents of raw moringa were 54.77%, 24.78%, 6.48%, and 9.84%, respectively, while NOCNF exhibited a higher content of holocellulose (60.3% - mostly cellulose) and much lower content of lignin (4.0%). The significant decrease in the non-cellulosic components after NOP confirmed its successful pulping function. We hypothesize that the residual lignin content in NOCNF might be due to the presence of lignin-

carbohydrate complexes, within which stable chemical bonds could resist the cleavage of β-O-4 ether bods in polyphenolic units.

Figure 2 illustrates the likely mechanism of selective cellulose oxidation by the nitro-oxidation process, which is a revised version from the one we proposed earlier. [21] In this mechanism, the reaction between $HNO_3$ and $NaNO_2$ generates $HNO_2$ and nitroxonium ions ($NO^+$), which can selectively attack primary hydroxyl group ($-CH_2OH$) of the cellulose unit at the $C_6$ position and produce $-CH(OH)_2$ group as the intermediate in the first oxidation circle. Subsequently, $-CH(OH)_2$ group can be continuously oxidized into carboxylic groups (-COOH) in the second oxidation circle. Overall, $NO^+$ as the oxidizing agent is gained and consumed during the reaction, where the end N-product is the mixture of $NO_X$ gases. Although the exact compositions of $NO_X$ gases have not yet been determined, we believe the byproducts will contain three different gases: NO, $NO_2$ and $N_2O$. NO nd $NO_2$ can be generated by he following reactions:

$$R\text{-}CH_2OH + HNO_3 \longrightarrow R\text{-}COOH + NO + H_2O$$

$$NO + 2HNO_3 \longrightarrow 3NO_2 + H_2O$$

In addition, $N_2O$ can be produced when HNO dissociates in water, as reported by Strojny.(Strojny, Iwamasa et al. 1971) In Figure 2, we only indicate $N_2O$ as a possible end N-product. Other gaseous products will also be possible, which will be experimentally verified in our future study.

***Characterization of NOCNF***

Figure 3(i) illustrates the FTIR spectra of raw moringa plant, extracted NOCNF and Hg-NOCNF floc after the remediation study. The FTIR spectrum of the moringa plant showed several distinctive peaks: 3328 $cm^{-1}$ corresponding to the -OH stretching and 2900 $cm^{-1}$ corresponding to the C-H symmetrical stretching in the cellulose unit; 1515 $cm^{-1}$ due to the C=C symmetrical stretching in the aromatic lignin unit; and 1739, 1602, 1460, 1240, and 810 $cm^{-1}$ in the xylan unit. In the FTIR spectrum of NOCNF, it was seen that both OH stretching peak at 3328 $cm^{-1}$ and C-H stretching peak at 2900 $cm^{-1}$ became much sharper than those in moringa plant, confirming the hypothesis that some removal of lignin and hemicellulose components took place resulting in the dominant presence of cellulose scaffold. The delignification function of NOP was further verified by the near absence of the 1515 $cm^{-1}$ peak form the lignin unit. However, the hemicellulose peaks at 1739, 1602, 1460, 1240, and 810 $cm^{-1}$ remained visible, suggesting that the removal of hemicellulose in NOCNF is only partial. This is reasonable as the hemicellulose component acts as a crosslinker between cellulose elementary microfibrils, which may not be accessible by the oxidation process.(Chi and Catchmark 2017) It is interesting to note that, the peak at 1602 $cm^{-1}$ due to the stretching motion in the carboxyl group was found to be notably increased in the NOCNF spectrum, verifying the modification of hydroxy group to carboxyl group in the anhydroglucose unit (probably at the C6 position) by NOP.

The WAXD pattern of the moringa plant in Figure 3(ii) showed a cellulose I structure with 2θ angles at 14.8, 16.7, 22.7 and 34.7°, corresponding to $(1\bar{1}0)$, (110), (200) and (004) reflection planes, respectively. The peaks at 14.8 and 16.7° were overlapped, which needed to be deconvoluted to reveal individual intensity and position. This is a quite common in higher plants with cellulose $I_\beta$ allomorph structure. For NOCNF, similar WAXD pattern was observed,

suggesting the cellulose crystalline structure was maintained during nitro-oxidation, which only performed the defibrillation process. However, the peak positions of $(1\bar{1}0)$ and (110) were found to shift to lower 2θ values (thus larger d-spacings), reflecting to the slight loosening of the crystalline structure due to cellulose oxidation. The crystallinity index (CI) values for the moringa plant and NOCNF were calculated by the peak height method (Equation S1, *Supporting Information),* and they were 61.2 and 67.3 %, respectively. The slight increase in the crystallinity of NOCNF was mainly due to the reduction of amorphous, non- cellulosic components (lignin) during the nitro-oxidation process.

The thermogravimetric (TGA) and derivative thermogravimetric (DTG) profiles of raw moringa plant and NOCNF are shown in Figures 3(iii) and 3(iv), respectively. The moringa plant showed the onset of thermal degradation ($T_{onset}$) at 174 °C with 9 wt% weight loss and the offset temperature ($T_{offset}$) was about 764 °C. In contrast, NOCNF exhibited $T_{onset}$ at 136 °C with 15 wt% weight loss and $T_{offset}$ at 802 °C. The lower $T_{onset}$ value in NOCNF confirmed the removal of more thermally stable lignin component by nitro-oxidization, resulting in the exposure of holocellulose part that is more vulnerable to thermal decomposition. In addition, the earlier initialization of thermal degradation of NOCNF was probably due to the presence of anhydroglucuronic acid units,(Sharma and Varma 2014, Sharma and Varma 2014) consisting of thermally unstable carboxyl groups.

The DTG curve of the moringa plant showed a primary peak at 302 °C, corresponding to the degradation of holocellulose moiety(Zhang, Zhao et al. 2013, Ornaghi Júnior, Zattera et al. 2014), and a secondary peak between 402-500 °C , related to the lignin moiety. In contrast, NOCNF

317 displayed two primary peaks (260 °C and 300 °C), which are characteristics of oxidized
318 nanocellulose, such as TEMPO-oxidized cellulose. The first peak is due to the decomposition of
319 the anhydroglucuronic acid units, where the surface carboxylate groups can initiate the
320 decarbonation and decarboxylation reactions when subjected to heating. The second peak
321 corresponds to the decomposition of residual un-modified cellulose moiety. In addition, a minor
322 peak in the temperature range of 400 - 430 °C was observed in NOCNF, suggesting the lignin
323 component was significantly removed during the nitro-oxidation process, which is consistent with
324 chemical composition results in Figure 1. Overall, the difference in thermal stability between
325 moringa and NOCNF can be attributed to their surface chemistry and degree of polymerization
326 (DP). After nitro-oxidation, a high amount of carboxyl groups is generated on the surface of
327 moringa cellulose, which can initiate the decarbonation and decarboxylation processes at low
328 temperatures. In addition, under the influence of nitric acid pulping and cellulose oxidation by
329 NOP, NOCNF's DP can be greatly reduced, resulting in more reducing ends and initiating sites
330 for depolymerization and decomposition.
331
332 The carboxylate content of resulting NOCNF was determined by the conductimetric titration
333 technique using Equation S2 in *Supporting Information*. The result indicated that the carboxylate
334 content of NOCNF was 0.97 mmol/g, which is comparable to NOCNF derived from jute biomass
335 as reported in our previous study.(Sharma, Sharma et al. 2020) The surface charge density of the
336 NOCNF sample was also verified by the zeta potential measurement (see description in the
337 *Supporting Information*), which yielded a negative zeta potential value of -59 mV confirming the
338 abundant content of $COO^-$ groups on the surface of NOCNF.
339

340 ***Morphological Evaluation***

341

342 A representative TEM image of NOCNF extracted from the moringa plant displayed the
343 nanofibrous morphology as shown in Figure 4(i). In this image, 20 individual fibers were identified
344 and used to estimate the fiber length and fiber width, which were 250-300 nm and 10-12 nm,
345 respectively. The AFM image (Figure 4(ii)) presented similar nanofibrous morphology in NOCNF,
346 where the height measurement indicated that the average fiber thickness was about 2.1 nm. This
347 indicated that the extracted NOCNF possessed a ribbon shape instead of the circular-like fiber
348 form. The representative SEM image of raw moringa sample is shown in Figure 4(iii), indicating
349 that the initial sample possessed a microscopic fiber form with width in the range of 20-100 µm
350 and several mini-meters in length. The morphological characterization of raw moringa fiber and
351 NOCNF clearly confirmed the effective extraction of cellulose fibers from raw biomass using the
352 nitro-oxidation process.

353

354 ***Characterization of NOCNF-Hg Floc***

355

356 The FTIR spectrum of the NOCNF-Hg floc sample is illustrated in Figure 3(i)c. In this spectrum,
357 a shift of the carboxylate peak in NOCNF from 1600 $cm^{-1}$ to 1635 $cm^{-1}$ in the NOCNF-Hg floc
358 was observed, probably due to the crosslinking between $Hg^{2+}$ ions and carboxylate ($COO^-$) groups
359 of NOCNF. However, we note that the intensity of 1635 $cm^{-1}$ can also be attributed to the presence
360 of the acetate group in the mercury acetate solution used in this study. Figure 5 illustrates the

361 photographs of the floc formation by mixing 100, 500 and 1000 ppm of $Hg^{2+}$ solutions with a
362 NOCNF suspension under neutral condition. It was observed that white flocs were immediately
363 formed, precipitated and settled down in the bottom of the tube in a very short period of time (less
364 than 20 s). This indicated that the NOCNF in the suspension form is an excellent adsorption and
365 coagulation agent, capable of finding with $Hg^{2+}$ ions, resulting in efficient removal of mercury
366 contaminant.
367

368 ***Mechanisms of Hg Removal by NOCNF in Suspension***

369

370 To understand the interactions between $Hg^{2+}$ ions and NOCNF in suspension, SEM and EDX
371 images of floc samples formed with different $Hg^{2+}$concentrations (250 ppm and 1000 ppm) are
372 shown in Figure 6. The two SEM images clearly exhibited the change in morphology of the
373 NOCNF-Hg floc with different amounts of $Hg^{2+}$. In Figure 6(i), at a low concentration of $Hg^{2+}$
374 (250 ppm), the floc surface was relatively uniform, where individual nanofibers could be
375 identified. However, the presence of Hg was also apparent in the EDS spectrum. As the $Hg^{2+}$
376 concentration increased to 1000 ppm, the floc surface became more aggregated, but the individual
377 fiber morphology disappeared. In fact, a few large aggregates were seen in otherwise a relatively
378 smooth surface. These aggregates could be attributed to the mineralization of HgO on the NOCNF
379 surface. The corresponding EDS spectrum confirmed the larger content of Hg in the NOCNF-Hg
380 floc (1000 ppm) than that in NOCNF-Hg (250 ppm). In addition to the presence of Hg, EDS also
381 showed the element of Na from the -COONa on NOCNF.
382

383 The different morphology of the NOCNF-Hg floc, containing varying amount of Hg adsorption,
384 indicates that the adsorption mechanisms between the $Hg^{2+}$ ions and NOCNF are quite different
385 when the $Hg^{2+}$ concentration changes. Based on the experimental results, we hypothesize that at
386 low $Hg^{2+}$ concentration (< 250 ppm), the $Hg^{2+}$ ion behaves like an ionic cross-linking agent,
387 capable of electrostatically interacting with two carboxylate groups ($COO^-$) on the NOCNF
388 surface. The binding of the $Hg^{2+}$ ions and carboxylate groups would lead to the neutralization of
389 NOCNF, resulting in further aggregation of NOCNF particles due to hydrophobic interactions. In
390 the NOCNF-Hg floc, the adsorbed/anchored Hg moiety appeared to act as a nucleation site for the
391 growth of mercury(II) oxide (HgO) nanocrystals on the surface of NOCNF. Most probably, the
392 low pH value of the system can facilitate the growth of HgO nanocrystals because the acidic pH
393 condition can hydrolyze mercury acetate and form unstable mercury hydroxide ($Hg(OH)_2$), which
394 subsequently loses water and becomes HgO.(Wang and Andrews 2005)
395
396 The mineralization of HgO nanocrystals was confirmed by WAXD measurement of the floc
397 (Figure 4(iii)), which will be explained later. The similar mineralization occurrence of nanocrystals
398 in the CNF scaffold during remediation has also been reported earlier.(Sharma, Chattopadhyay et
399 al. 2017, Sharma, Chattopadhyay et al. 2018, Sharma, Chattopadhyay et al. 2018) To understand
400 the HgO mineralization mechanism in this study, the pH values of the different Hg solution (at
401 varying concentration) before and after remediation using NOCNF were first measured, and the
402 results are summarized in Table S1. It was seen that the pH value decreased upon the increase in
403 the Hg concentration. For example, at the Hg concentration of 2.5 ppm, the pH value of the solution
404 was 5.02; while at the concentration of 1000 ppm, the pH value was 3.44. The decrease in pH was
405 due to the increase in acetate ions ($CH_3COO^-$) in the solution, formed by dissociation of mercury

406 acetate. Upon the addition of NOCNF, the same decreasing trend of the pH value was seen with
407 the increase in Hg concentration, but the decrease in pH was stopped at 4.66 when 1000 ppm of
408 Hg solution was used. Notably, no mineralization and precipitation were observed with increasing
409 Hg concentration in the absence of NOCNF. The above finding indicates that NOCNF is playing
410 a crucial role by providing the active site for adsorption and mineralization of $Hg^{2+}$, leading to
411 high removal efficiency against $Hg^{2+}$ ions.
412

413 The hydrophobicity of the floc sample containing 1000 ppm of $Hg^{2+}$ was analyzed by the contact
414 angle measurement, and the results are shown in Figure 7(i) (the inset image). This NOCNF-Hg
415 floc sample was found to possess a contact angle of 114.5°, indicating that the Hg adsorption
416 neutralized the charge on NOCNF resulting in a hydrophobic composite (the as extracted NOCNF
417 has a contact angle about 38° (Sharma, Chattopadhyay et al. 2018)). The WAXD measurement of
418 the NOCNF-Hg floc sample was carried out to examine its crystal nature. The results are displayed
419 in Figure 7(iii), where the WAXD profile of NOCNF is also included for comparison. It was found
420 that after remediation with 1000 ppm of $Hg^{2+}$, additional diffraction peaks appeared at $2\theta$ of 30.8,
421 32.3, 33.4, 38.3 and 50.9°, which could be indexed as the (011), (110), (020), (101) and (121)
422 lattice planes of HgO crystals (i.e., the orthorhombic phase of HgO with a space group of Imm2;
423 JCPDS No. 72-1141).(Mohadesi, Ranjbar et al. 2014) This evidence supports the growth of HgO
424 nanocrystals in the NOCNF scaffold which is also in agreement with the SEM results from the
425 floc sample at 1000 ppm of Hg concentration (Figure 6(ii)). The TEM image of the floc sample
426 with 1000 ppm of Hg concentration is shown in Figure 7(i). Compared to the disperse fiber image
427 of NOCNF (Figure 4(i)), the NOCNF-Hg floc exhibited an aggregated form of nanofiber network
428 containing inorganic nanocrystals shown as black dots in TEM. These black dots, uniformly

dispersed in the fiber aggregate, are associated with the mercury oxide (HgO) particles. This was proven by the electron diffraction measurement of the floc sample, where the result is shown in Figure 7(ii). The electron diffraction patterns of the floc sample showed five strong diffraction rings that could also be indexed as the (011), (110), (020), (101), (121) planes, as shown in WAXD (Figure 7(iii)). We note that in the TEM study, no staining agent was used while preparing the sample; this ensured the absence of any other metal ions except merury.

***Assessment of $Hg^{2+}$ Adsorption Mechanism by NOCNF Suspension***

The behavior of $Hg^{2+}$ adsorption by NOCNF was evaluated in the Hg concentration range of 2.5 ppm to 1000 ppm. The ICP-MS results were used to calculate the *Qe* value (i.e., the experimental adsorption capacity of NOCNF) and *Ce*/*Qe* ratio (i.e., the original $Hg^{2+}$ concentration of NOCNF divided by the experimental adsorption capacity of $Hg^{2+}$ ions at equilibrium per gram of NOCNF in suspension). It was found that the adsorption efficiency of $Hg^{2+}$ by NOCNF decreased from 88.5% to 47.2% when the Hg concentration increased from 2.5 to 1000 ppm. Meanwhile, the experimental capacity raised from 0.55 mg/g to 117.9 mg/g. Using Eq.1, the plot of *Ce*/*Qe versus Ce* was fitted with the Langmuir adsorption model, and the result is illustrated in Figure 8(i). The value of *Qe* was calculated by multiplying the adsorption efficiency of NOCNF by the ideal adsorption capacity of NOCNF. The results of the ideal adsorption capacity and the experimental capacity of NOCNF are summarized in Table S2 in the *Supplementary Information*. In addition, the Freundlich adsorption model was also employed to predict the isotherm of $Hg^{2+}$ remediation process. The plot of lg(*Qe*) *versus* lg(*Ce*) fitted by the Freundlich equation (Eq. 2) is shown in Figure 8(ii). The fitting parameters, such as the slope and R square value, of these two models are

summarized in Table 1. Both models exhibited very high R square values: 0.9946 for the Langmuir model, and 0.9951 for the Freundlich model. These results suggest that the adsorption mechanism cannot truly be differentiated based on the different model analysis. Nevertheless, from the analysis of the Langmuir model, the *Qm* value (the maximum adsorption capacity of the adsorbent) could be calculated, i.e., 257.07 mg/g, which is higher than most adsorbents reported.(Anoop Krishnan and Anirudhan 2002, Puanngam and Unob 2008, Tran, Wu et al. 2015, Anbia and Amirmahmoodi 2016, Guo, Wang et al. 2017, Sajjadi, Mohammadzadeh et al. 2018)

***Effect of pH and Time on $Hg^{2+}$ Remediation by NOCNF Suspension***

The pH effect on $Hg^{2+}$ remediation was carried out to assess the removal efficiency of NOCNF in suspension, and the results are summarized in Table S3 in *Supporting Information* and in Figure 8(iii). It was observed that the removal efficiency increased to 88.9 % when the pH value increased from 3 to 9. The reason that at pH=9, the highest removal efficiency was obtained is because the maximum negative charge density of NOCNF could be induced by the deprotonation of carboxyl group ($COO^-$) at alkaline conditions. With a further increase in the pH value to 11, NOCNF showed a decrease in the removal efficiency to 75.6%. This is because the further increase in pH, the condition might start to degrade NOCNF. In contrast, the removal efficiency of NOCNF at pH=3 was only 35.9 %,. This is because the acidic conditions could protonate the carboxylate groups on the NOCNF surface, resulting in an acid form (COOH) with less binding sites available to interact with the $Hg^{2+}$ ions. The above study clearly indicates the pH-dependent characteristic of NOCNF for mecury removal, as the NOCNF suspension can be considered as a weak polyelectrolyte due to the carboxylate group on the particle surface.

475

476 The effect of time on the $Hg^{2+}$ remediation by NOCNF suspension was also evaluated, and the
477 results are shown in Figure 8(iv). It was found that there was no significant change in the removal
478 efficiency when the experiments were performed between 3 h to 24 h. The removal efficiency was
479 stabilized between 81.1 - 81.6 %, indicating that the removal of $Hg^{2+}$ by NOCNF took place mainly
480 in the initial hours of the remediation study. This study shows that a swift remediation process can
481 be achieved by using NOCNF suspension as a mercury removal agent.

482

483 ***Comparison with Other Adsorbents***

484

485 The comparison of the maximum adsorption capacity (*Qm*) of different adsorbents for mercury
486 removal is listed in Table 2. Compared to nanomaterials, such as thiol and hydroxyl containing
487 montmorillonite(Tran, Wu et al. 2015), nanoporous carbon grafted with surfacants(Anbia and
488 Amirmahmoodi 2016), and chemically-modified MCM-41 and silica gel(Puanngam and Unob
489 2008), NOCNF extracted from moringa plants showed the highest maximum adsorption capacity
490 value of 257 mg/g in the Hg concentration range of 2.5-1000 ppm. In Table 2, some natural
491 biomaterials, such as coconut husk(Guo, Wang et al. 2017) and activated carbon(Sajjadi,
492 Mohammadzadeh et al. 2018) prepared from different sources have also been included. Among
493 them, one activated carbon presented very good maximum adsorption capacity value of 202 mg/g,
494 although in a very narrow Hg concentration range of 2.5-4.5 ppm. The activated carbon(Anoop
495 Krishnan and Anirudhan 2002) prepared from bagasse pith also exhibited good maximum
496 adsorption capacity of 172 mg/g in a wider Hg concentration range of 50-1000 ppm. But these
497 values are still smaller than that of NOCNF. We believe the good performance of NOCNF should

498 be independent of the biomass source used. The remarkable mercury removal property of NOCNF
499 in suspension is due to its high surface area, large carboxylate concentration and unique scaffolding
500 capability to induce HgO mineralization.

501

502 ***Filtration Column using Freeze-Dried NOCNF***

503

504 NOCNF suspensions were also freeze-dried into dry powder samples as adsorbent materials in
505 filtration column for the evaluation of mercury removal. In this study, 3 g of dried NOCNF sample
506 was packed into a column of 15 cm in length. Subsequently, 100 ppm of $Hg^{2+}$ solution was passed
507 through the column slowly by gravity. The output $Hg^{2+}$ solution was collected and tested by the
508 ICP-MS technique, where the results are shown in Table 3. It was seen that the removal efficiency
509 achieved by this gravity-driven column in the first pas of the study was 74.3%, but the removal
510 efficiency began to decrease upon further addition of the $Hg^{2+}$ solution. With the total passing of
511 150 mL filtrate (10 additions of 15 ml $Hg^{2+}$ solution) through the column, the removal efficiency
512 was found to be 53.3 %. The decrease in the removal efficiency of the column was due to the
513 saturation of carboxyl groups on the NOCNF surface through binding with $Hg^{2+}$ ions. It was seen
514 that the adsorption results from the use of NOCNF suspension indicated the removal efficiency of
515 81.6% at the Hg concentration of 100 ppm (Table S2 in *Supplementary Information*), which is
516 higher than the removal efficiency by using solid NOCNF in filtration column. This can be
517 explained as follows. During freeze drying process, the aggregation of nanocellulose can occur
518 due to the increasing interfibrillar interactions (van der Waal forces and hydrogen bonding),
519 leading to reduced surface area and decreasing binding sites for $Hg^{2+}$ ions in the NOCNF scaffold.
520 In the filtration column application, the primary adsorption mechanism is dominated by the

electrostatic interactions between carboxylate groups and the $Hg^{2+}$ ions, where the mineralization process probably does not occur. To improve the total removal efficiency of the column, one needs to increase the total carboxylate content of the adsorbent by raising: (1) the degree of CNF oxidation, (2) the total loading of NOCNF, and (3) the surface area of NOCNF. Furthermore, we argue although the removal efficiency of solid NOCNF is not as good as NOCNF in suspension, the transportation cost of the formal may be much more cost-effective than the latter.

## Conclusions

This work demonstrates an effective nanocellulose-based adsorbent system (in suspension or solid form) for mercury removal that was developed from untreated moringa plant using the nitro-oxidation method. The structure, property and functionality of the resulting NOCNF was thoroughly characterized by SEM, TEM, AFM, FTIR, WAXD, TGA and DTG techniques. The nitro-oxidation method appears to be a useful approach that can extract nanocellulose adsorbents from many other raw biomass sources. The present mercury remediation study using NOCNF comprises of three major activities to investigate (i) the adsorption mechanism of NOCNF in suspension against $Hg^{2+}$ ions; (2) the effects of pH and time on the adsorption capacity and removal efficiency of $Hg^{2+}$ by NOCNF; and (3) the deployment of NOCNF suspension as an adsorbent/coagulant system, and of solid NOCNF adsorbent in filtration column. In the mechanism study, it was found that at low $Hg^{2+}$ concentrations (< 250 ppm), the removal mechanism was dominated by electrostatic interactions between $Hg^{2+}$ and $COO^-$ on the NOCNF surface; at high $Hg^{2+}$ concentrations (> 1000 ppm), the removal mechanism was dominated by the mineralization process of HgO crystal formation in the NOCNF scaffold. As a result of the mineralization, the

544 maximum adsorption capability of NOCNF for the $Hg^{2+}$ removal at pH = 7 was 257.07 mg/g,
545 which was the highest among all mercury adsorbents reported thus far. Finally, we observed that
546 the removal efficiency by the NOCNF suspension was higher than that of the solid NOCNF
547 adsorbent in filtration column as expected. However, the practical depolyment value for each
548 system will depend on the detailed techno-economic assessment of the technology that is also
549 location dependent.
550
551 **Acknowledgement**
552
553 The financial support for this work was provided by a grant from the Polymer Program of the
554 Division of Materials Science in the National Science Foundation (DMR-1808690). The authors
555 thank Drs. Chung-Chueh Chang and Yuan Xue at the Advanced Energy Research and Technology
556 Center in Stony Brook University for the assistance of the TGA, TEM and AFM measurements,
557 and Ms. Katie Wooton at the Facility for Isotope Research and Student Training in Stony Brook
558 University for the assistance of the ICP-MS analysis.
559
560

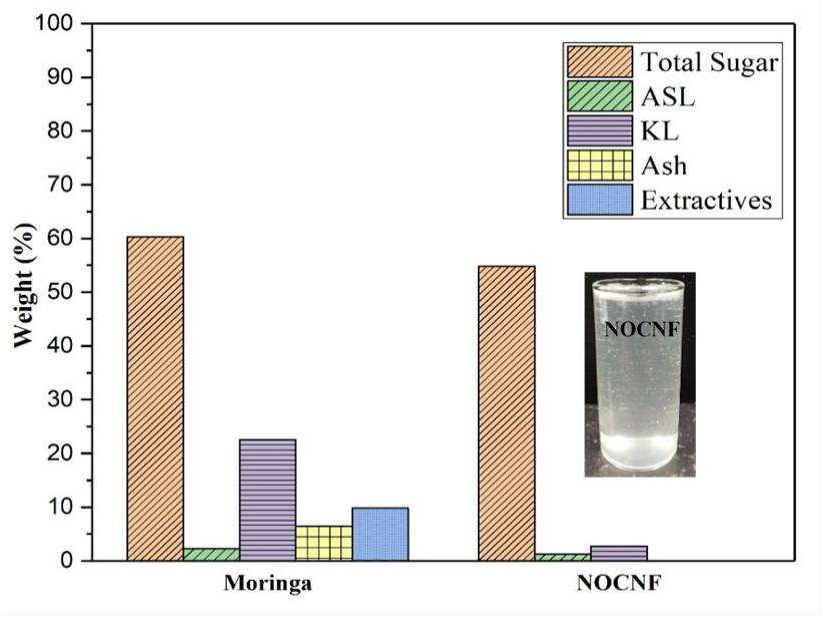


561

562 **Figure 1.** Chemical compositions of raw moringa and extracted NOCNF (ASL: acid soluable
563 lignin, KL: klason lignin). The inset image is the 0.4 wt NOCNF suspension that exhibits the
564 viscous and gel-like behavior).

565

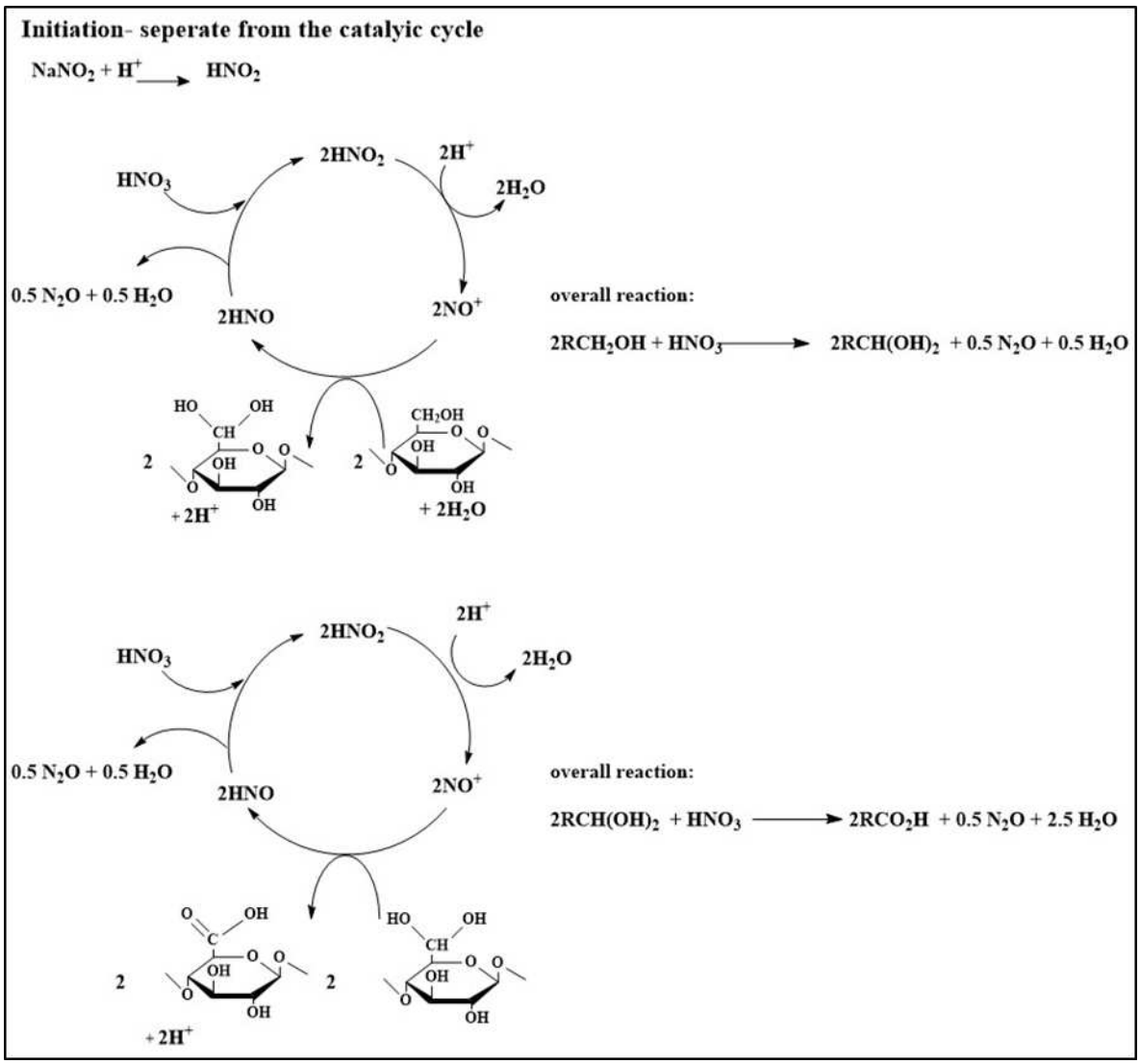


**Figure 2.** Proposed cellulose oxidation mechanisms by the nitro-oxidation method.

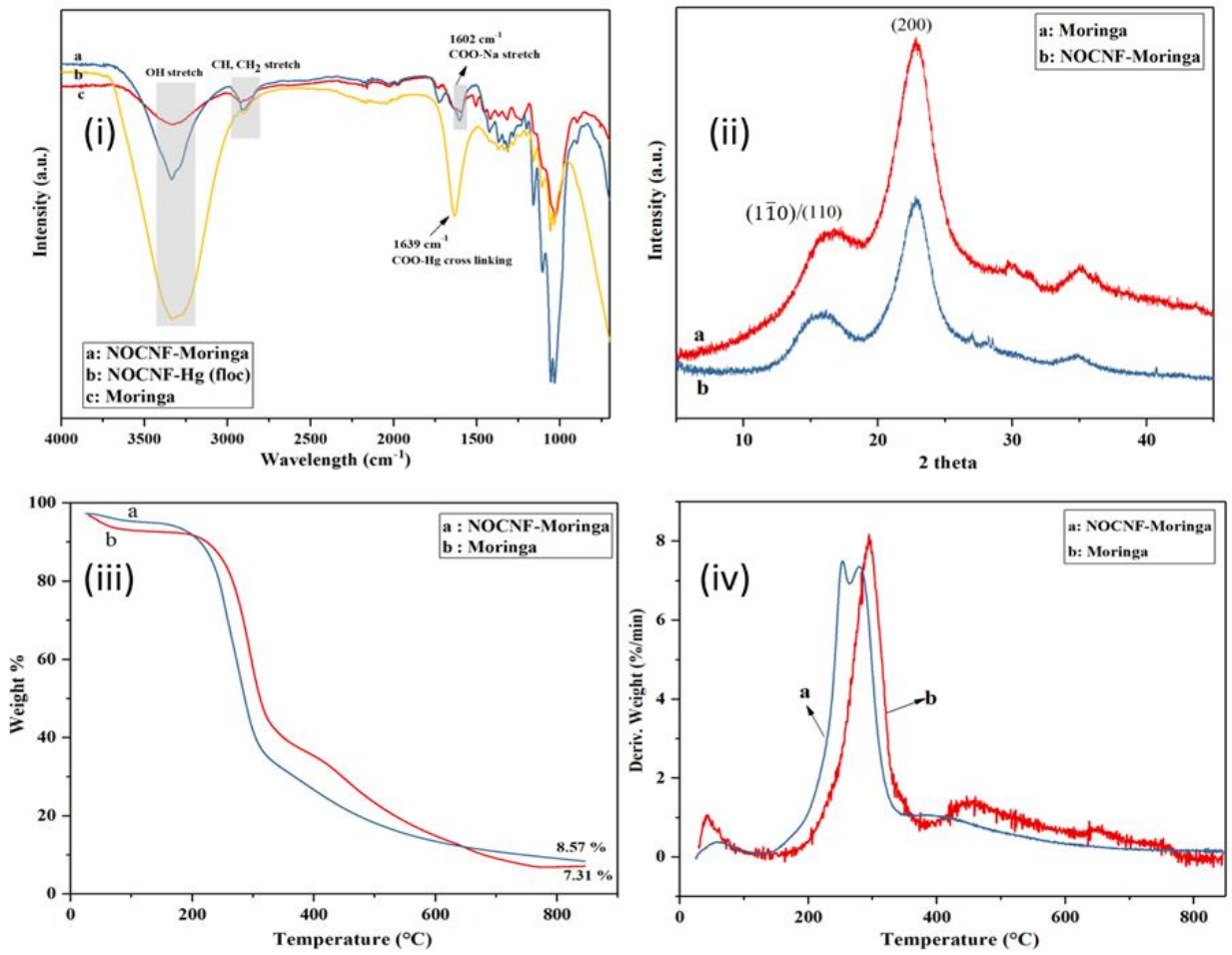


**Figure 3.** Characterization of raw moringa plant, NOCNF and NOCNF-Hg floc: (i) FTIR of raw moringa plant (red curve), NOCNF (blue curve) and NOCNF-Hg floc (yellow curve); (ii) WAXD paterns of raw moringa plant (red curve) and NOCNF (blue curve); (iii) TGA curves of raw moringa plant (red curve) and NOCNF (blue curve); (iv) Derivative Thermogravimetric (DTG) curve of raw moringa plant (red curve) and NOCNF (blue curve).

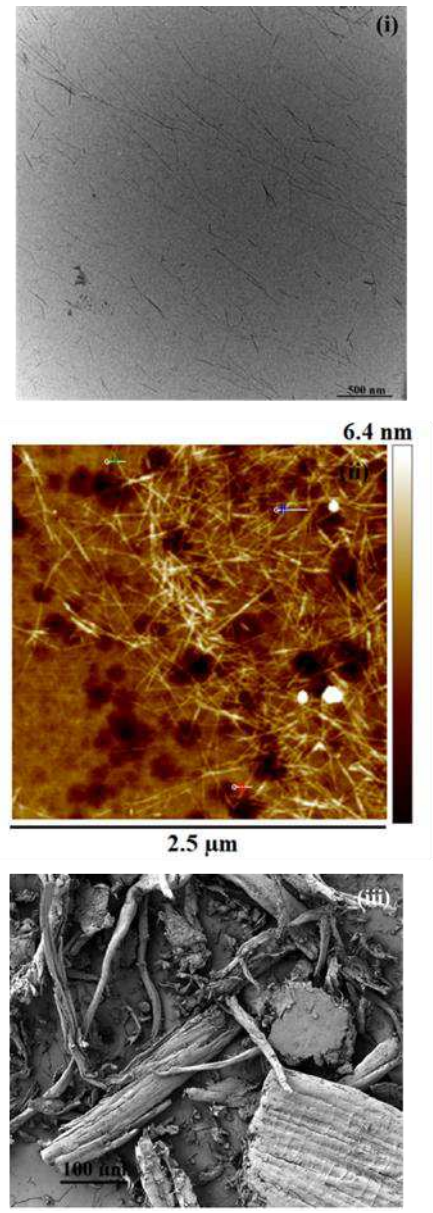


576

577 **Figure 4.** Morphological charcterization: (i) TEM and (ii) AFM images of NOCNF, (iii) SEM
578 image of crushed moringa fibers.

579

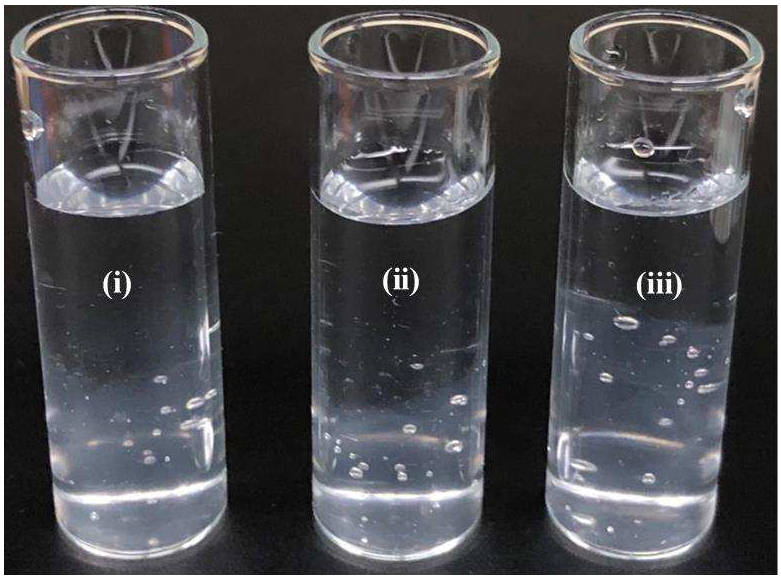


580

581 **Figure 5**. Photographs of suspensions NOCNF-Hg floc, formed by mixing of (i) 100 ppm, (ii)

582 500 ppm and (iii) 1000 ppm of $Hg^{2+}$ solutions with a 0.4 wt% NOCNF suspension.

583

584 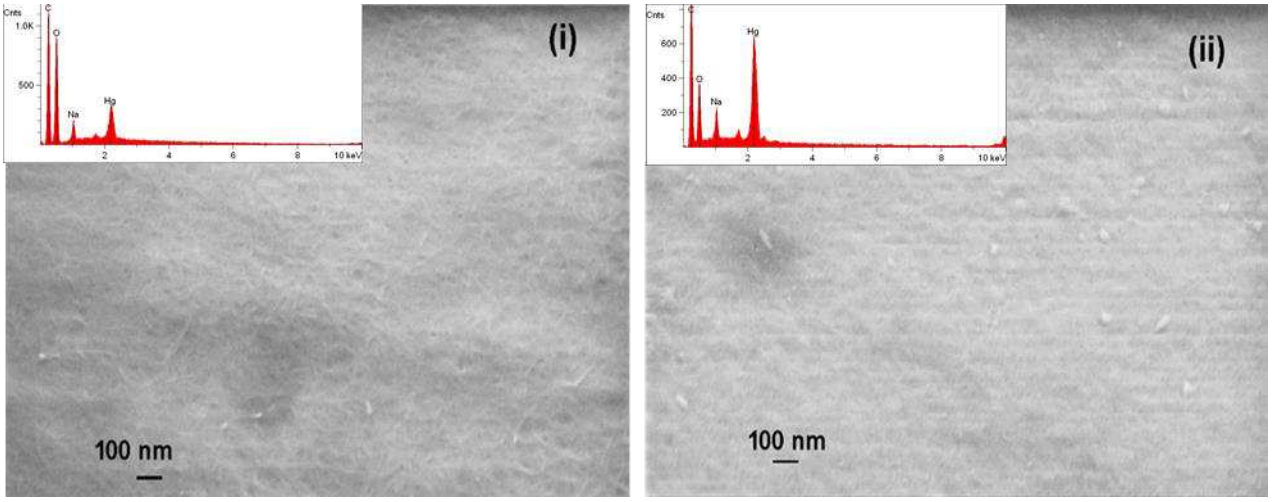


585 **Figure 6.** SEM images with EDS spectra (the insert) of NOCNF-Hg floc formed by using (i) 250

586 ppm and (ii) 1000 ppm of $Hg^{2+}$ solutions.

587

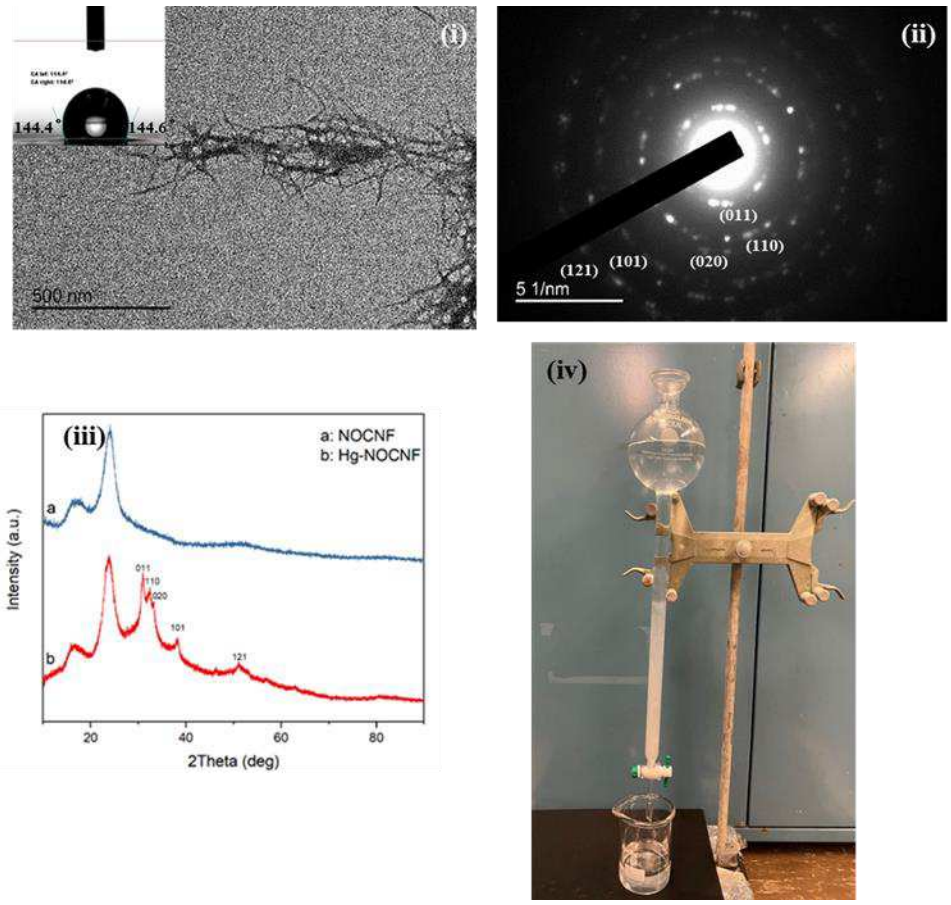


588

589 **Figure 7.** Characterization of the NOCNF-Hg floc: (i) TEM image of the floc; the inset
590 represents the contact angle of the floc, (ii) electron diffraction image of the floc, (iii) WAXD
591 profiles of NOCNF and NOCNF-Hg floc (formed by mixing of 0.32 wt% NOCNF suspension
592 and 1000 ppm $Hg^{2+}$ solution at the volume ratio of 1:1 ), and (iv) the setup of the filtration
593 column.

594

595

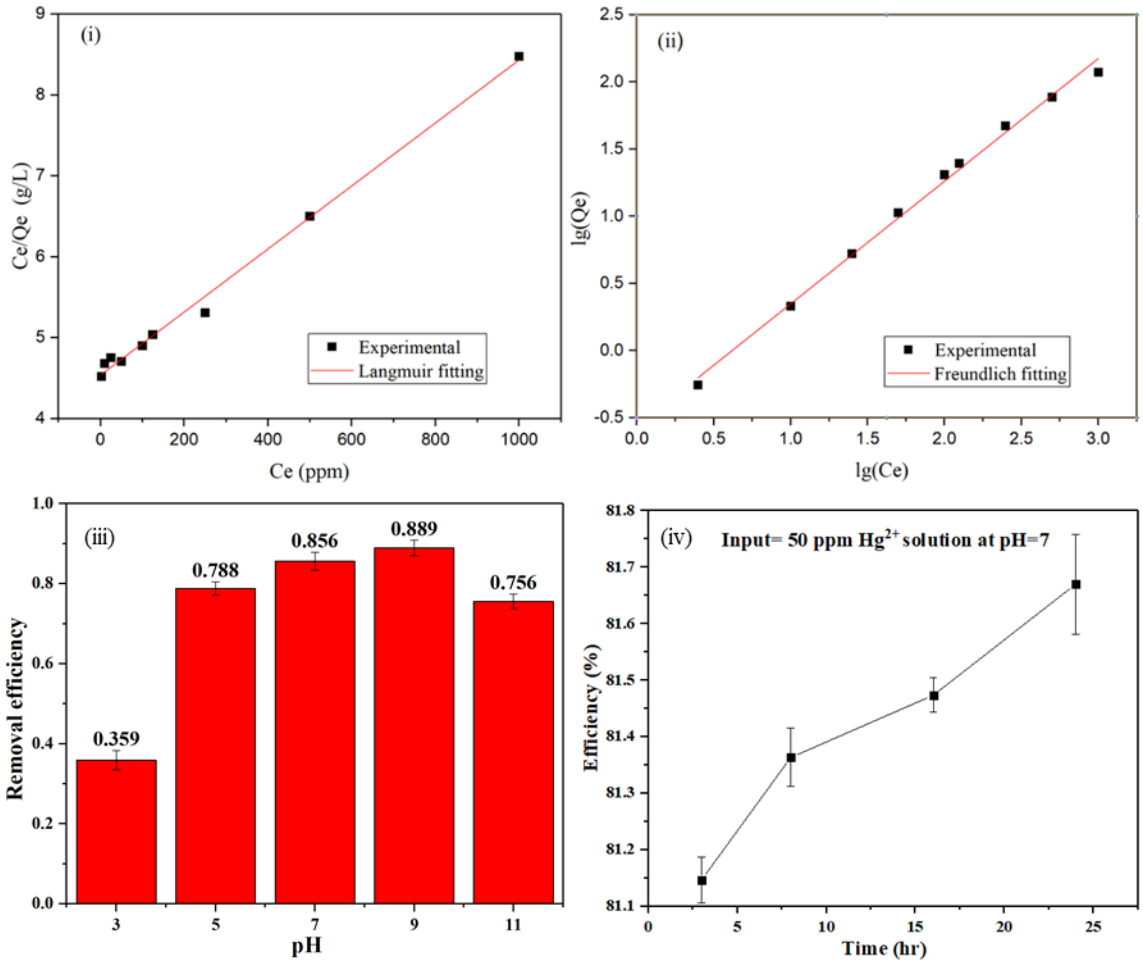


596

597 **Figure 8.** (i) The $Hg^{2+}$ adsorption data by using the NOCNF suspension as an adsorbent (the
598 $Hg^{2+}$ concentration was ranged between 2.5 to 1000 ppm) analyzed by the Langmuir model, (ii)
599 the adsorption data analyzed by the Freudlich model, (iii) the effect of pH on the removal
600 efficiency and; (iv) the effect of time on the $Hg^{2}$ removal efficiency by NOCNF at 100 ppm $Hg^{2+}$
601 concentration at pH=7.

602

603

604 **Table 1.** Summary of the Langmuir and Freundlich fitting model parameters.

| | **Langmuir** | | **Freundlich** | |
|---|---|---|---|---|
| Equation | y=0.00389x+4.538 | | y=0.91338x-0.565 | |
| $R^2$ | 0.9946 | | 0.9951 | |
| Parameters | ***b*** | ***Qm* (mg/g)** | ***n*** | $K_f$ |
| Value | 0.00086 | 257.07 | 1.095 | 3.673 |

605

606

607 **Table 2.** Comparison of the maximum adsorption capacity of varying adsorbents reported in the
608 literature and NOCNF in this study against the $Hg^{2+}$ removal.
609

| Adsorbents | Maximum adsorption capacity *Qm* (mg/g) | Adsorption range (ppm) | Reference |
|---|---|---|---|
| Thiol and hydroxyl containing montmorillonite | 8.57 | <100 | [(Tran, Wu et al. 2015)] |
| Nanoporous carbon impregnated with surfactants | 8.9 | 10-200 | [(Anbia and Amirmahmoodi 2016)] |
| MCM-41-NH-L | 152 | 100-800 | [(Puanngam and Unob 2008)] |
| Silica gel | 140 | 100-800 | [(Puanngam and Unob 2008)] |
| Coconut husk | 44.9 | 40-450 | [(Guo, Wang et al. 2017)] |
| Activated carbon from pistachio wood waste | 202 | 2.5-45 | [(Sajjadi, Mohammadzadeh et al. 2018)] |
| Activated carbon from bagasse pitch | 172 | 50-1000 | [(Anoop Krishnan and Anirudhan 2002)] |
| NOCNF from moringa plant | 257.1 | 2.5-1000 | This study |

610
611

612 **Table 3.** Results from filtration column using NOCNF for $Hg^{2+}$ removal.

613

| Column label | Input concentration (ppm) | Filtrate ICP-MS concentration (ppb) | Filtrate concentration (ppm) | Efficiency |
|---|---|---|---|---|
| 1 | 100 | 25.7 | 25.70 | 0.743 |
| 2 | 100 | 26.5 | 26.50 | 0.735 |
| 3 | 100 | 31.1 | 31.10 | 0.689 |
| 4 | 100 | 31.6 | 31.60 | 0.684 |
| 5 | 100 | 33 | 33.00 | 0.670 |
| 6 | 100 | 34.8 | 34.80 | 0.652 |
| 7 | 100 | 35.5 | 35.50 | 0.645 |
| 8 | 100 | 40.4 | 40.40 | 0.596 |
| 9 | 100 | 42.5 | 42.50 | 0.575 |
| 10 | 100 | 46.7 | 46.70 | 0.533 |

614

615

616

# References


Anbia, M. and S. Amirmahmoodi (2016). "Removal of Hg (II) and Mn (II) from aqueous solution using nanoporous carbon impregnated with surfactants." Arabian Journal of Chemistry **9**: S319-S325.

Anoop Krishnan, K. and T. S. Anirudhan (2002). "Removal of mercury(II) from aqueous solutions and chlor-alkali industry effluent by steam activated and sulphurised activated carbons prepared from bagasse pith: kinetics and equilibrium studies." Journal of Hazardous Materials **92**(2): 161-183.

Baeyens, W. R. G., R. Ebinghaus, O. F. Vasil'ev, N. A. R. W. o. Regional, F. Global Mercury Cycles: Sources and B. Mass (1997). "Global and regional mercury cycles : sources, fluxes and mass balances."

Chen, H., S. K. Sharma, P. R. Sharma, H. Yeh, K. Johnson and B. S. Hsiao (2019). "Arsenic(III) Removal by Nanostructured Dialdehyde Cellulose–Cysteine Microscale and Nanoscale Fibers." ACS Omega **4**(26): 22008-22020.

Chi, K. and J. M. Catchmark (2017). "The influences of added polysaccharides on the properties of bacterial crystalline nanocellulose." Nanoscale **9**(39): 15144-15158.

Chiarle, S., M. Ratto and M. Rovatti (2000). "Mercury removal from water by ion exchange resins adsorption." Water Research **34**(11): 2971-2978.

Cui, G., M. Liu, Y. Chen, W. Zhang and J. Zhao (2016). "Synthesis of a ferric hydroxide-coated cellulose nanofiber hybrid for effective removal of phosphate from wastewater." Carbohydrate Polymers **154**: 40-47.

Di Natale, F., A. Erto, A. Lancia and D. Musmarra (2011). "Mercury adsorption on granular activated carbon in aqueous solutions containing nitrates and chlorides." Journal of Hazardous Materials **192**(3): 1842-1850.

Guo, Y., Z. Wang, X. Zhou and R. Bai (2017). "Removal of mercury (II) from aqueous solution with three commercial raw activated carbons." Research on Chemical Intermediates **43**(4): 2273-2297.

Harada, M. (1995). "Minamata Disease: Methylmercury Poisoning in Japan Caused by Environmental Pollution." Critical Reviews in Toxicology **25**(1): 1-24.

International Symposium on Metals Speciation, S., Recovery, J. W. Patterson, R. Passino, C. Industrial Waste Elimination Research and a. Istituto di ricerca sulle Metals speciation, separation, and recovery, Chelsea, MI, Lewis Publishers.

Kalibbala, H., O. Wahlberg and T. Hawumba (2009). "The impact of Moringa oleifera as a coagulant aid on the removal of trihalomethane (THM) precursors and iron from drinking water." Water Science and Technology: Water Supply **9**(6): 707-714.

Kim, J.-H., B. S. Shim, H. S. Kim, Y.-J. Lee, S.-K. Min, D. Jang, Z. Abas and J. Kim (2015). "Review of nanocellulose for sustainable future materials." International Journal of Precision Engineering and Manufacturing-Green Technology **2**(2): 197-213.

Lai, E. P. C., B. Wong and V. A. VanderNoot (1993). "Preservation of solid mercuric dithizonate samples with polyvinyl chloride for determination of mercury(II) in environmental waters by photochromism-induced photoacoustic spectrometry." Talanta **40**(7): 1097-1105.

Larson, K. A. and J. M. Wiencek (1992). "Liquid ion exchange for mercury removal from water over a wide pH range." Industrial & Engineering Chemistry Research **31**(12): 2714-2722.

Liu, P., K. Oksman and A. P. Mathew (2016). "Surface adsorption and self-assembly of Cu(II) ions on TEMPO-oxidized cellulose nanofibers in aqueous media." Journal of Colloid and Interface Science **464**: 175-182.

Melesse, A. and K. Berihun (2013). "Chemical and mineral compositions of pods of Moringa stenopetala and Moringa oleifera cultivated in the lowland of Gamogofa Zone." Journal of Environmental and Occupational Science **2**: 1.

Mohadesi, A., M. Ranjbar and S. M. Hosseinpour-Mashkani (2014). "Solvent-free synthesis of mercury oxide nanoparticles by a simple thermal decomposition method." Superlattices and Microstructures **66**: 48-53.
Nam, K. H., S. Gomez-Salazar and L. L. Tavlarides (2003). "Mercury(II) Adsorption from Wastewaters Using a Thiol Functional Adsorbent." Industrial & Engineering Chemistry Research **42**(9): 1955-1964.
Ornaghi Júnior, H. L., A. J. Zattera and S. C. Amico (2014). "Thermal behavior and the compensation effect of vegetal fibers." Cellulose **21**(1): 189-201.
Puanngam, M. and F. Unob (2008). "Preparation and use of chemically modified MCM-41 and silica gel as selective adsorbents for Hg(II) ions." Journal of Hazardous Materials **154**(1): 578-587.
Rio, S. and A. Delebarre (2003). "Removal of mercury in aqueous solution by fluidized bed plant fly ash." Fuel **82**(2): 153-159.
Sajjadi, S.-A., A. Mohammadzadeh, H. N. Tran, I. Anastopoulos, G. L. Dotto, Z. R. Lopičić, S. Sivamani, A. Rahmani-Sani, A. Ivanets and A. Hosseini-Bandegharaei (2018). "Efficient mercury removal from wastewater by pistachio wood wastes-derived activated carbon prepared by chemical activation using a novel activating agent." Journal of Environmental Management **223**: 1001-1009.
Sehaqui, H., A. Mautner, U. Perez de Larraya, N. Pfenninger, P. Tingaut and T. Zimmermann (2016). "Cationic cellulose nanofibers from waste pulp residues and their nitrate, fluoride, sulphate and phosphate adsorption properties." Carbohydrate Polymers **135**: 334-340.
Sharma, P., A. Chattopadhyay, C. Zhan, S. Sharma, L. Geng and B. Hsiao (2018). "Lead removal from water using carboxycellulose nanofibers prepared by nitro-oxidation method." Cellulose **25**.
Sharma, P. R., A. Chattopadhyay, S. K. Sharma, L. Geng, N. Amiralian, D. Martin and B. S. Hsiao (2018). "Nanocellulose from Spinifex as an Effective Adsorbent to Remove Cadmium(II) from Water." ACS Sustainable Chemistry & Engineering **6**(3): 3279-3290.
Sharma, P. R., A. Chattopadhyay, S. K. Sharma and B. S. Hsiao (2017). "Efficient Removal of UO22+ from Water Using Carboxycellulose Nanofibers Prepared by the Nitro-Oxidation Method." Industrial & Engineering Chemistry Research **56**(46): 13885-13893.
Sharma, P. R., R. Joshi, S. K. Sharma and B. S. Hsiao (2017). "A Simple Approach to Prepare Carboxycellulose Nanofibers from Untreated Biomass." Biomacromolecules **18**(8): 2333-2342.
Sharma, P. R., S. K. Sharma, W. Borges, H. Chen and B. S. Hsiao (2020). Remediation of UO<sub>2</sub> <sup>2+</sup> from Water by Nitro-Oxidized Carboxycellulose Nanofibers: Performance and Mechanism. Contaminants in Our Water: Identification and Remediation Methods, American Chemical Society. **1352:** 269-283.
Sharma, P. R. and A. J. Varma (2014). "Functionalized celluloses and their nanoparticles: morphology, thermal properties, and solubility studies." Carbohydrate polymers **104**: 135-142.
Sharma, P. R. and A. J. Varma (2014). "Thermal stability of cellulose and their nanoparticles: Effect of incremental increases in carboxyl and aldehyde groups." Carbohydrate Polymers **114**: 339-343.
Sharma, P. R., B. Zheng, S. K. Sharma, C. Zhan, R. Wang, S. R. Bhatia and B. S. Hsiao (2018). "High Aspect Ratio Carboxycellulose Nanofibers Prepared by Nitro-Oxidation Method and Their Nanopaper Properties." ACS Applied Nano Materials **1**(8): 3969-3980.
Sharma, S. K., P. R. Sharma, H. Chen, K. Johnson, C. Zhan, R. Wang and B. Hsiao (2020). Cellulose-Supported Nanosized Zinc Oxide: Highly Efficient Bionanomaterial for Removal of Arsenic from Water. Contaminants in Our Water: Identification and Remediation Methods, American Chemical Society. **1352:** 253-267.
Sharma, S. K., P. R. Sharma, S. Lin, H. Chen, K. Johnson, R. Wang, W. Borges, C. Zhan and B. S. Hsiao (2020). "Reinforcement of Natural Rubber Latex Using Jute Carboxycellulose Nanofibers Extracted Using Nitro-Oxidation Method." Nanomaterials **10**(4): 706.

Skubal, L. R. and N. K. Meshkov (2002). "Reduction and removal of mercury from water using arginine-modified TiO2." Journal of Photochemistry and Photobiology A: Chemistry **148**(1): 211-214.
Sluiter, A., B. Hames, R. Ruiz, C. Scarlata, J. Sluiter, D. Templeton and D. Crocker (2010). "Determination of structural carbohydrates and lignin in biomass." Laboratory analytical procedure(TP-510-42618).
Strojny, E. J., R. Iwamasa and L. K. Frevel (1971). "Oxidation of 2-methoxyethanol to methoxyacetic acid by nitric acid solutions." Journal of the American Chemical Society **93**(5): 1171-1178.
Suman, A. Kardam, M. Gera and V. K. Jain (2015). "A novel reusable nanocomposite for complete removal of dyes, heavy metals and microbial load from water based on nanocellulose and silver nano-embedded pebbles." Environmental Technology **36**(6): 706-714.
Thakur, V. K. and S. I. Voicu (2016). "Recent advances in cellulose and chitosan based membranes for water purification: A concise review." Carbohydrate Polymers **146**: 148-165.
Tran, L., P. Wu, Y. Zhu, S. Liu and N. Zhu (2015). "Comparative study of Hg(II) adsorption by thiol- and hydroxyl-containing bifunctional montmorillonite and vermiculite." Applied Surface Science **356**: 91-101.
Wang, D. (2019). "A critical review of cellulose-based nanomaterials for water purification in industrial processes." Cellulose **26**(2): 687.
Wang, J.-W. and Y.-M. Kuo (2007). "Preparation of fructose‐mediated (polyethylene glycol/chitosan) membrane and adsorption of heavy metal ions." Journal of Applied Polymer Science **105**: 1480-1489.
Wang, R., S. Guan, A. Sato, X. Wang, Z. Wang, R. Yang, B. S. Hsiao and B. Chu (2013). "Nanofibrous microfiltration membranes capable of removing bacteria, viruses and heavy metal ions." Journal of Membrane Science **446**: 376-382.
Wang, X. and L. Andrews (2005). "Infrared Spectrum of Hg(OH)2 in Solid Neon and Argon." Inorganic Chemistry **44**(1): 108-113.
Zabihi, M., A. Ahmadpour and A. H. Asl (2009). "Removal of mercury from water by carbonaceous sorbents derived from walnut shell." Journal of Hazardous Materials **167**(1): 230-236.
Zhang, F.-S., J. O. Nriagu and H. Itoh (2005). "Mercury removal from water using activated carbons derived from organic sewage sludge." Water Research **39**(2): 389-395.
Zhang, X., Z. Zhao, G. Ran, Y. Liu, S. Liu, B. Zhou and Z. Wang (2013). "Synthesis of lignin-modified silica nanoparticles from black liquor of rice straw pulping." Powder Technology **246**: 664-668.
Zhu, C., I. Dobryden, J. Rydén, S. Öberg, A. Holmgren and A. P. Mathew (2015). "Adsorption Behavior of Cellulose and Its Derivatives toward Ag(I) in Aqueous Medium: An AFM, Spectroscopic, and DFT Study." Langmuir **31**(45): 12390-12400.

# Figures

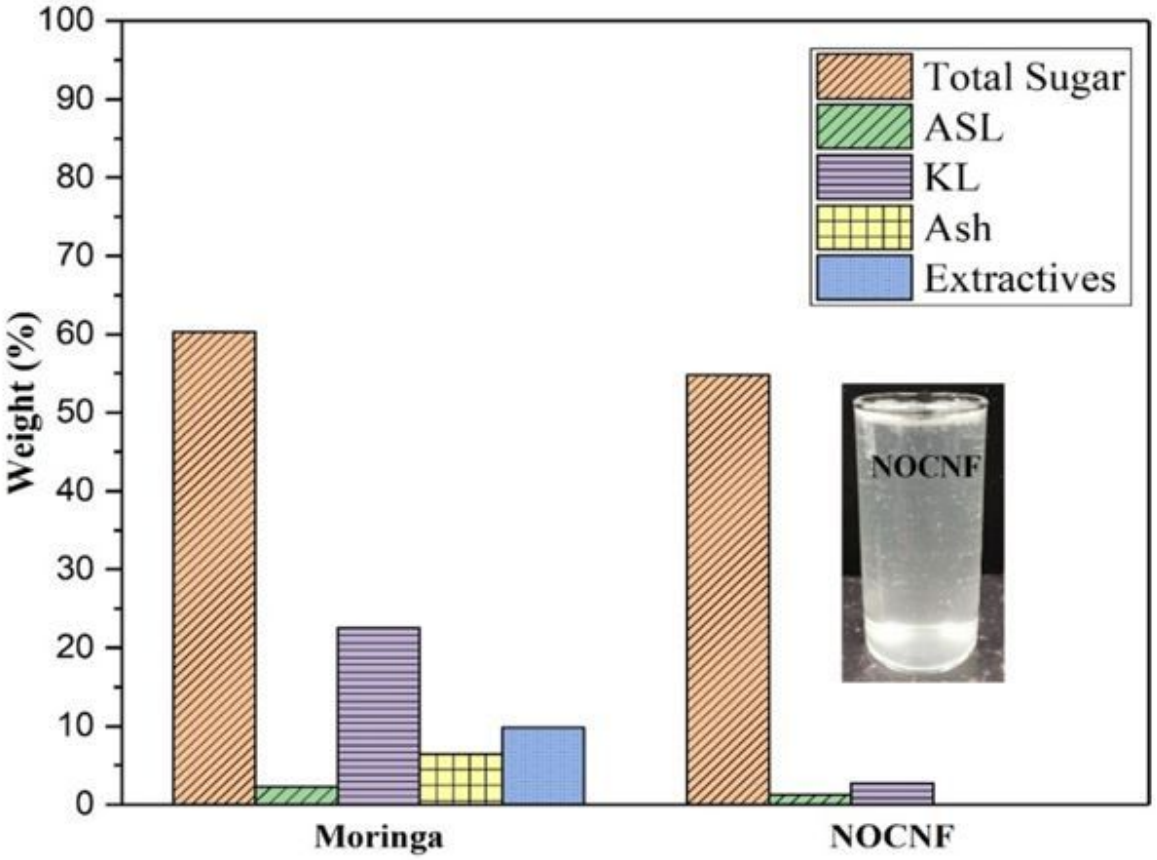


**Figure 1**

Chemical compositions of raw moringa and extracted NOCNF (ASL: acid soluable lignin, KL: klason lignin). The inset image is the 0.4 wt NOCNF suspension that exhibits the viscous and gel-like behavior).

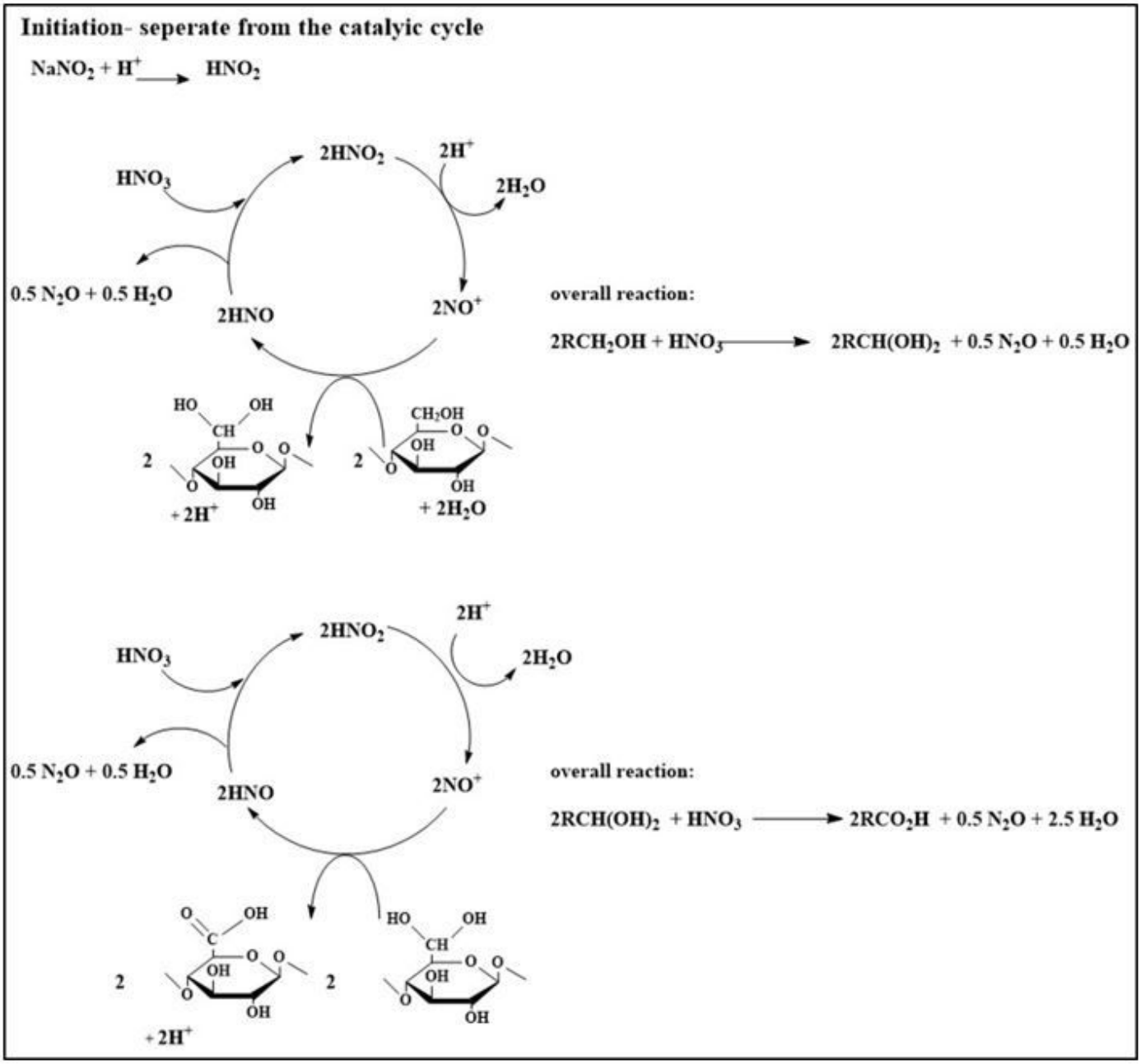


## Figure 2

Proposed cellulose oxidation mechanisms by the nitro-oxidation method.

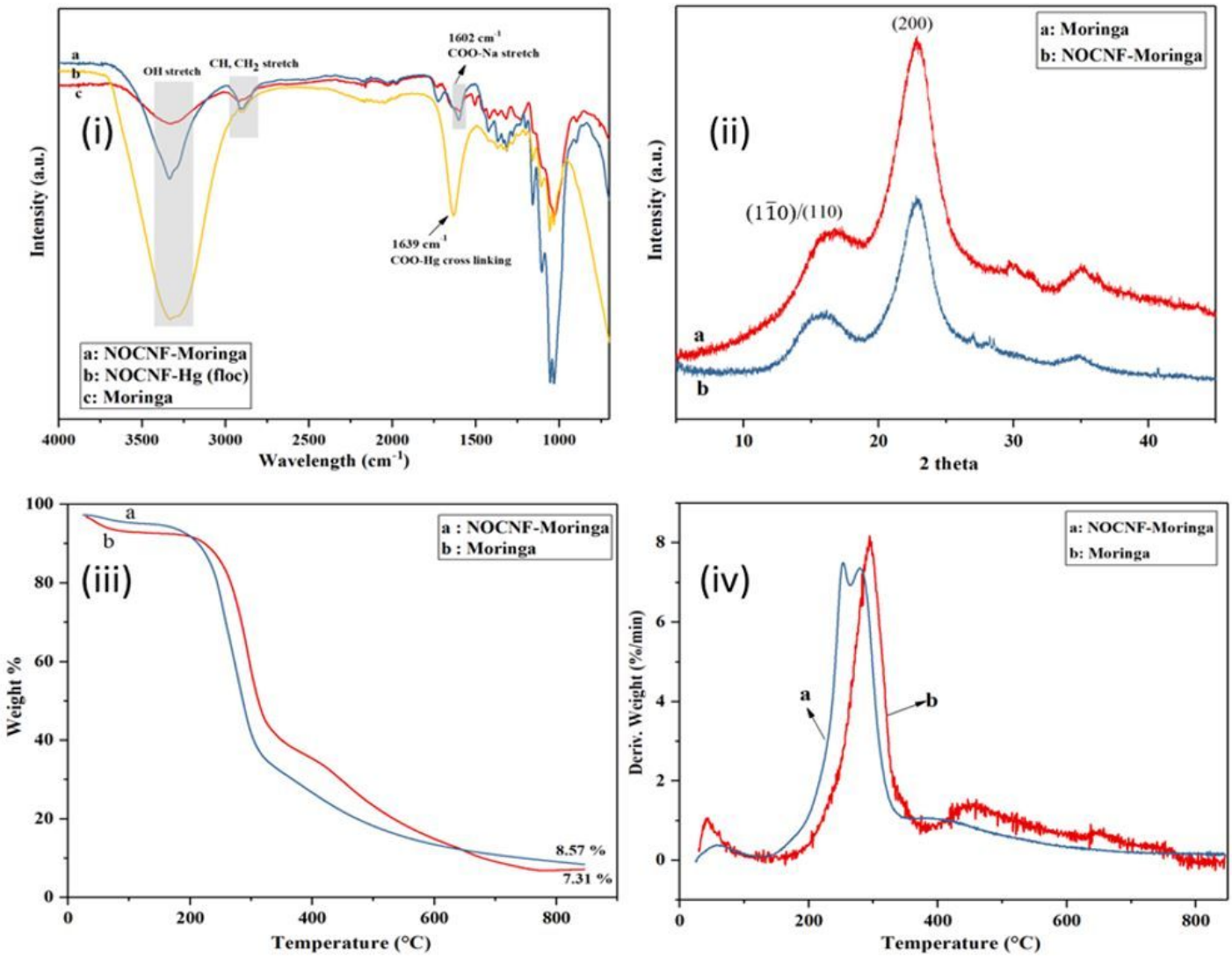


## Figure 3

Characterization of raw moringa plant, NOCNF and NOCNF-Hg floc: (i) FTIR of raw moringa plant (red curve), NOCNF (blue curve) and NOCNF-Hg floc (yellow curve); (ii) WAXD paterns of raw moringa plant (red curve) and NOCNF (blue curve); (iii) TGA curves of raw moringa plant (red curve) and NOCNF (blue curve); (iv) Derivative Thermogravimetric (DTG) curve of raw moringa plant (red curve) and NOCNF (blue curve).

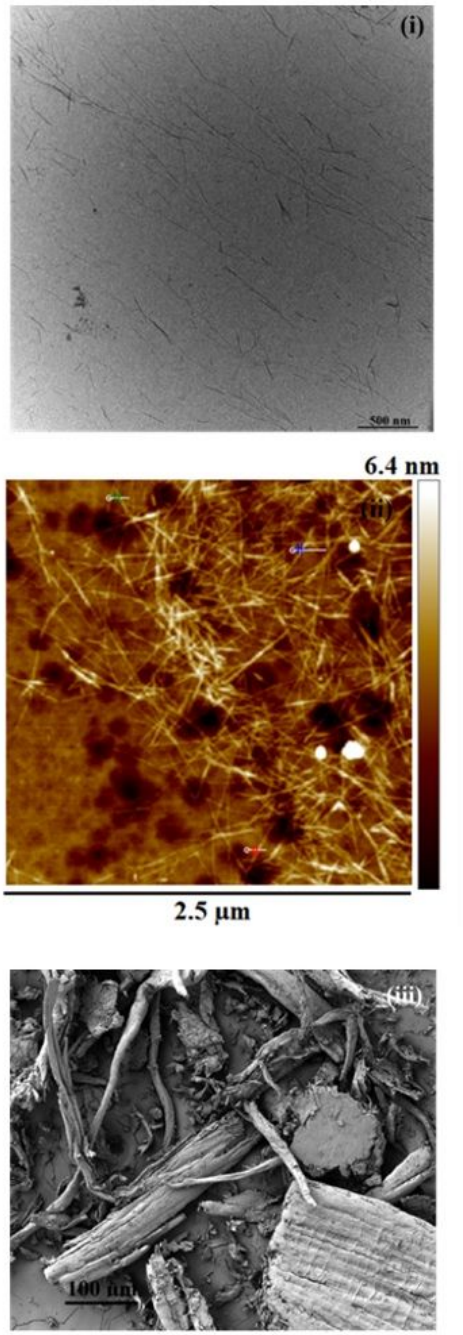


## Figure 4

Morphological charcterization: (i) TEM and (ii) AFM images of NOCNF, (iii) SEM image of crushed moringa fibers.

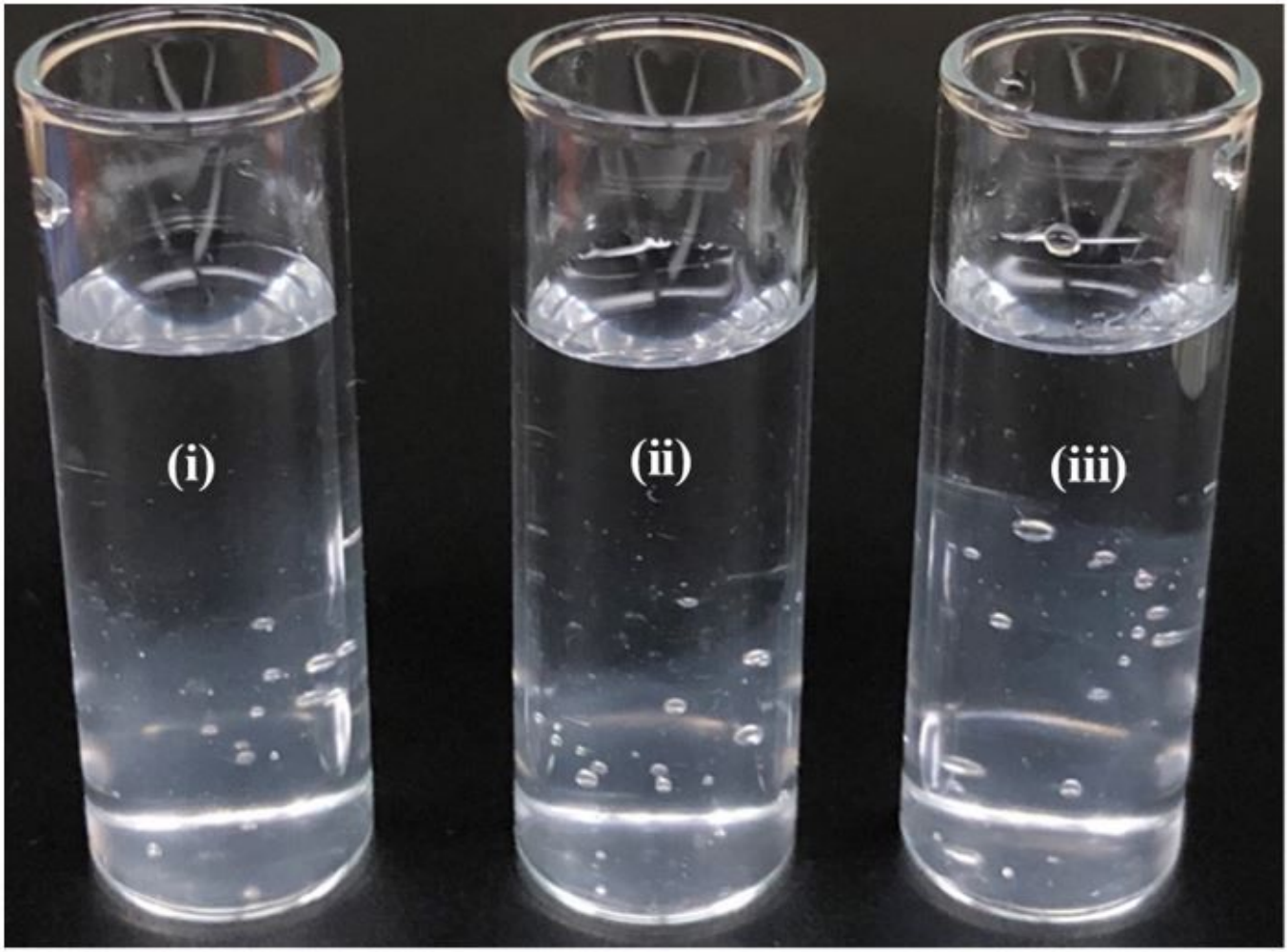


**Figure 5**

Photographs of suspensions NOCNF-Hg floc, formed by mixing of (i) 100 ppm, (ii) 500 ppm and (iii) 1000 ppm of Hg2+ solutions with a 0.4 wt% NOCNF suspension.

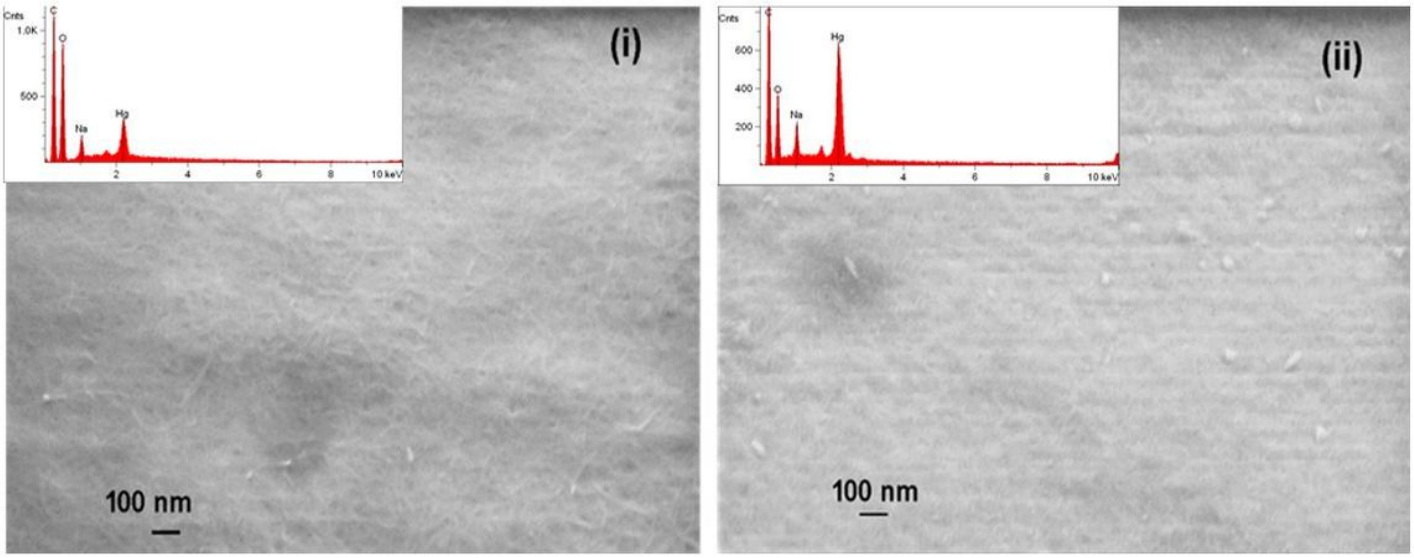


**Figure 6**

SEM images with EDS spectra (the insert) of NOCNF-Hg floc formed by using (i) 250 ppm and (ii) 1000 ppm of Hg2+ solutions.

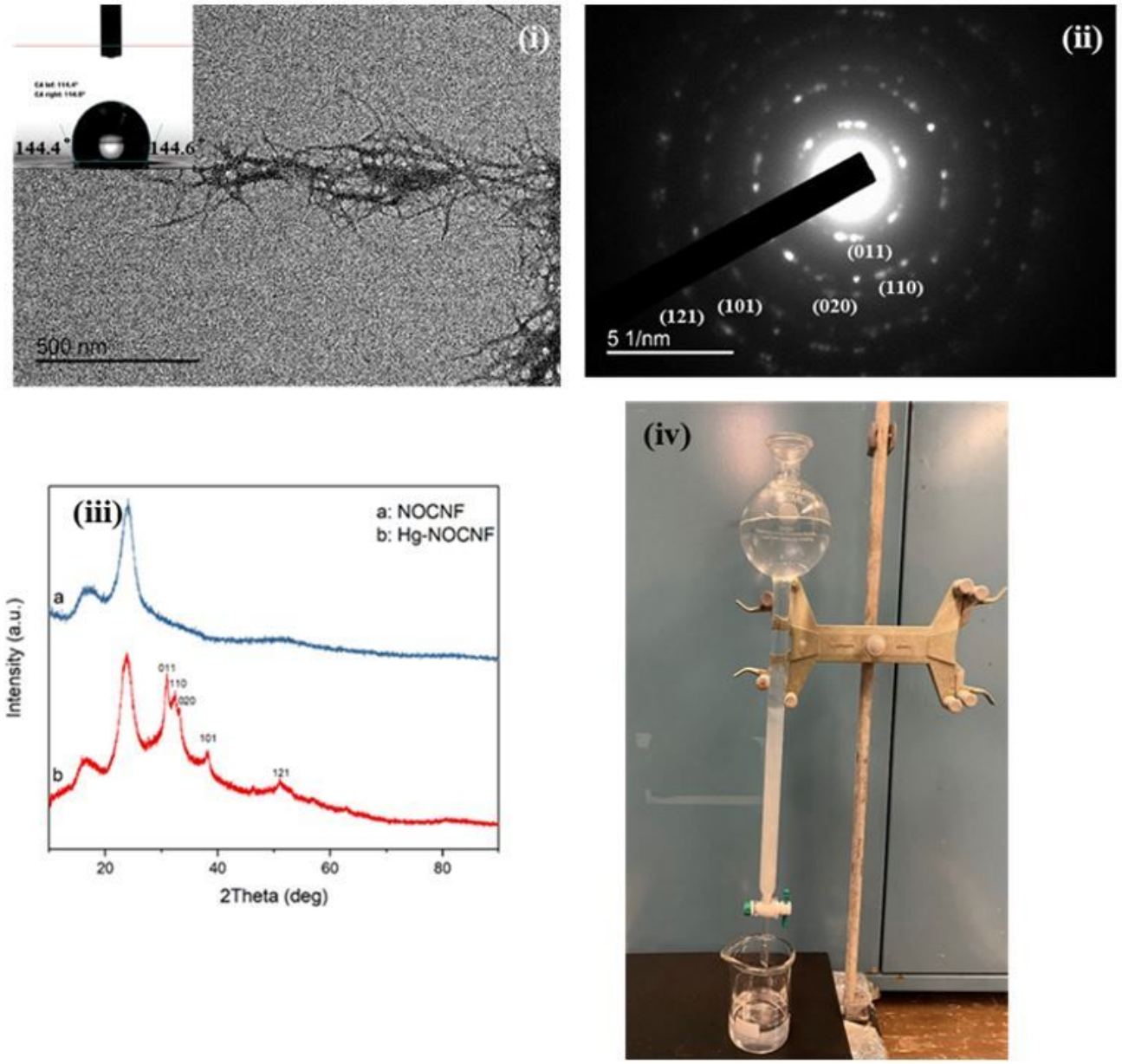


## Figure 7

Characterization of the NOCNF-Hg floc: (i) TEM image of the floc; the inset represents the contact angle of the floc, (ii) electron diffraction image of the floc, (iii) WAXD profiles of NOCNF and NOCNF-Hg floc (formed by mixing of 0.32 wt% NOCNF suspension and 1000 ppm Hg2+ solution at the volume ratio of 1:1 ), and (iv) the setup of the filtration column.

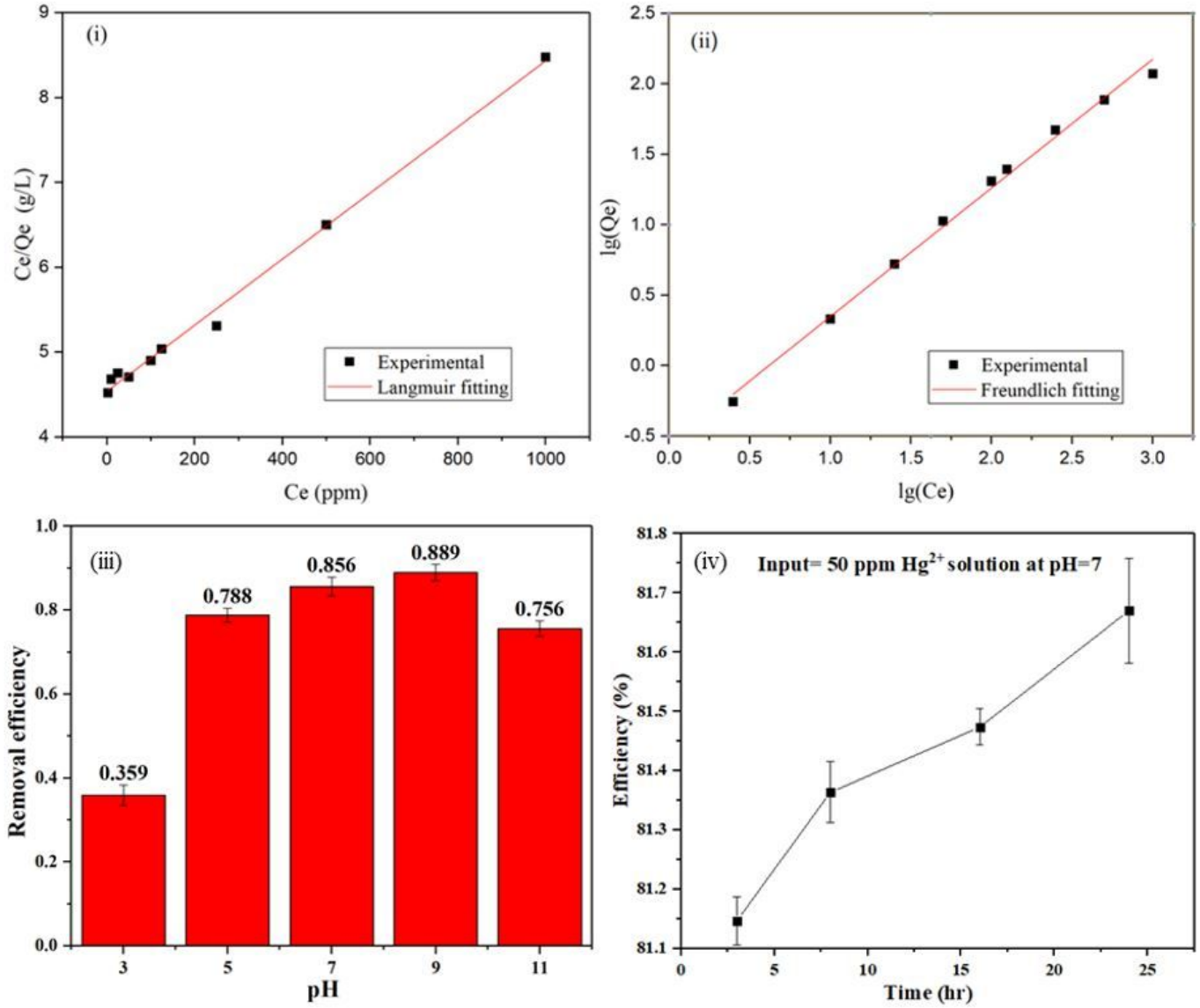


**Figure 8**

(i) The Hg2+ adsorption data by using the NOCNF suspension as an adsorbent (the Hg2+ concentration was ranged between 2.5 to 1000 ppm) analyzed by the Langmuir model, (ii) the adsorption data analyzed by the Freudlich model, (iii) the effect of pH on the removal efficiency and; (iv) the effect of time on the Hg2 removal efficiency by NOCNF at 100 ppm Hg2+ concentration at pH=7.

# Supplementary Files

This is a list of supplementary files associated with this preprint. Click to download.

- MercurysupplementaryInformationHuiChen.docx